Supplementary Information

Sustainable Waste-Nitrogen Upcycling Enabled by Low-Concentration Nitrate Electrodialysis and High-Performance Ammonia Electrosynthesis

Yifu Chen,[a] Pouya Ammari-Azar,[b] Hengzhou Liu,[a] Jungkuk Lee,[a] Yu Xi,[a] Michael J. Castellano,[c] Shuang Gu [*b] and Wenzhen Li [*a]

[a.] Department of Chemical and Biological Engineering, Iowa State University, Ames, Iowa 50011, USA

[b.] Department of Mechanical Engineering, Wichita State University, Wichita, Kansas 67260, USA

[c.] Department of Agronomy, Iowa State University, Ames, Iowa 50011, USA

*Corresponding authors: shuang.gu@wichita.edu (S. Gu), wzli@iastate.edu (W. Li)

Table of Contents

1. Experimental Section

1.1 Chemicals

All chemicals were used as received without purification. Nickel wire mesh (200 mesh, 0.002" wire diameter) was purchased from Wire Mesh Store. Nickel foam (1.6 mm thickness, 99.9%) was purchased from MTI Corporation. Nickel wire (0.04" diameter, 99.5%) and nickel rod (0.12" diameter, 99%) were purchased from Alfa Aesar. Sodium hydroxide (NaOH, ≥98%), potassium hydroxide (KOH, ≥85%), and the chemicals for the screening tests (Fig. 6b) were purchased from Sigma-Aldrich. Potassium nitrate (KNO_3, 99.7%), sulfuric acid (H_2SO_4, TraceMetal™ Grade), and ammonium hydroxide ($NH_3 \cdot H_2O$, 28.0–30.0 w/w %) were purchased from Fisher Chemical. Potassium nitrite (KNO_2, 97%) was purchased from Acros Organics. Protein powder (Orgain) was purchased from Amazon. Dry algae powder was kindly provided by Gross-Wen Technologies. Ammonia standard solution (100 mg L^{-1} as NH_3-N) was purchased from Hach. Plain carbon cloth (1071 HCB) and carbon paper (Sigracet 22 BB) were purchased from Fuel Cell Store. A201 anion exchange membrane (28 μm thickness) and AS-4 ionomer solution (5 wt.%) were purchased from Tokuyama Corporation. 40% Pt on Vulcan XC-72 (Pt/C) and 40% Pt-Ir (1:1 atomic ratio) on Vulcan XC-72 (PtIr/C) were purchased from Premetek. Nitrogen (N_2, Ultra High Purity, 99.999%), argon (Ar, Ultra High Purity, 99.999%), helium (He, Ultra High Purity, 99.999%), oxygen (O_2, Ultra High Purity, 99.999%), air (Industrial Grade), and carbon dioxide (CO_2, industrial grade) were purchased from Airgas. Deionized (DI) water (18.2 MΩ cm, Barnstead™ E-Pure™) was used for all experiments in this work.

1.2 Electrochemical Measurements for NH₃ Production

1.2.1 Operation of the Membrane-Free Alkaline Electrolyzer (MFAEL)

The configuration of MFAEL was modified from our previous work.[1] In brief, the cell body consisted of a 100 mL screw-cap polytetrafluoroethylene (PTFE) bottle (height: 88 mm; diameter: 52 mm) and a custom-made stainless-steel lid. Two pieces of 1/4" OD alumina ceramic tubes were used for the carrier gas inlet and outlet. A union tee with a septum was connected to the gas inlet tube and offered a liquid injection port, through which water or sample solution can be supplied during cell operation. Two 10 cm² nickel mesh electrodes (3.3 × 3 cm², 200 mesh) were used as the electrodes, and were attached to nickel wires (0.04" diameter) connected to a potentiostat (WaveDriver 20, for $I \leq 1000$ mA) or a DC power supply (BK Precision 1697B, for $I > 1000$ mA). Silicone O-rings and aluminosilicate adhesive (Resbond 907GF) were used to seal the gaps and ensure the cell installation is leak-free.

Prior to the electrolysis, the NaOH/KOH/H₂O electrolyte (containing equimolar of NaOH and KOH and 40 wt.% of water) was prepared by adding 29.7 g of NaOH, 48.1 g of KOH, and 38.9 g of deionized water in the PTFE bottle, which was then sealed in an oven at 80 °C overnight for the complete dissolution of NaOH and KOH. For typical tests, an appropriate amount of N-containing reactant was added before the cell cap was installed. For electrochemical NO_3^- reduction (NO3RR), the amount of added KNO_3 was equal to the theoretical amount of NO_3^- that can be fully converted to NH₃ based on the applied charge. For the conversion of organic Nr compounds, the amount of added reactant was specified in the figure captions. Subsequently, the cell was placed in an oil bath preheated to 80 °C, and 200 mL min^{-1} of N_2 was bubbled from the gas inlet tube into the electrolyte. The outlet gas from MFAEL was bubbled into an acidic absorbing solution (100 mL of 0.1 M H_2SO_4) for NH₃ collection.

After 30 min of gas bubbling to remove the air from the system, a constant current was applied between the electrodes. During electrolysis, the absorbing solution was changed every 30 min for NH_4^+ quantification. After electrolysis, the system was kept with gas bubbling for additional 30 min to deplete the remaining NH_3 in the gas line. The electrolyte was then carefully diluted to 1 L with deionized water for the quantification of NO_3^-, NO_2^-, and organic products (detailed in 1.5).

The conversion of NO_3^- (X) and faradaic efficiency of product i (FE_i) were calculated by

$$X = \frac{n_0 - n}{n_0} \times 100\%$$

$$FE_i = \frac{n_i z_i F}{Q} \times 100\%$$

where n_0 is the initial amount of NO_3^- (mol); n is the amount of NO_3^- after electrolysis (mol); n_i is the amount of product i (mol); z_i is the number of electrons transferred to product i; F is the Faraday constant (96,485 C mol^{-1}); Q is the total charge passed through the electrolytic cell (C).

The NH_3 production rate was calculated by

$$rate \ (mol \ cm^{-2} \ s^{-1}) = \frac{cV}{At}$$

where c is the NH_4^+ concentration (M); V is the volume of the absorbing solution (L); A is the geometric area of the electrode (cm^2); t is the electrolysis duration (s).

The N balance for Nr conversion was calculated by

$$N \ balance \ (\%) = \frac{amount \ of \ detected \ N \ species \ after \ reaction}{amount \ of \ added \ Nr} \times 100\%$$

For the real N-containing samples (protein and algae powder), the content of N (wt.%) was determined by a Combustion Elemental Analyzer (CHN/S Thermo FlashSmart 2000).

1.2.2 Measurement of Roughness Factor (RF)

To compare the electrochemically active surface area of the Ni-based electrodes before and after electrolysis in the NaOH/KOH/H$_2$O electrolyte, cyclic voltammetry (CV) measurements were carried out in a single-compartment cell with a standard three-electrode configuration without stirring.[2] The electrolyte was 1 M KOH. The geometric area of the working electrode was 1 cm^2 (1 × 1 cm^2). An Ag/AgCl electrode (saturated KCl, $E^0 = 0.197$ V $vs.$ SHE) and a Pt foil were used as the reference electrode and counter electrode, respectively. Different scan rates ranging from 50 to 200 mV s^{-1} were applied.

1.2.3 NO3RR in the Scaled-up MFAEL

The configuration of the scaled-up MFAEL is similar to the 100 mL reactor. The cell body consisted of a 2.5 L screw-cap PTFE bottle (height: 260 mm; diameter: 131 mm), a custom-made stainless-steel lid, two pieces of 1/2" OD alumina ceramic tubes, two 100 cm^2 nickel mesh electrodes (10 × 10 cm^2, 200 mesh), and two nickel rods (0.12" diameter) for conducting electricity. The nickel rods were bent and stitched through the folded nickel mesh electrodes to ensure stable contact, and were connected to a DC power supply (BK Precision 1901B). Silicone O-rings and aluminosilicate adhesive (Resbond 907GF) were used to seal the gaps and ensure the cell installation is leak-free. The amount of electrolyte was 25 times higher than the 100 mL reactor, and the amount of added KNO$_3$ was equal to the theoretical amount of NO_3^- that can be fully converted to NH_3 based on the applied charge. The flow rate of carrier gas was 500 mL min^{-1}. The

applied current was 25 A (corresponding to 250 mA cm^{-2} of current density), and the electrolysis time was 24 hours.

Different absorbing solutions were used for obtaining different NH$_3$-based chemical products. For NH$_4^+$ salts, 400 mL of 5 M H$_2$SO$_4$ was used for NH$_3$ absorption. For producing pure NH$_3$ solution, 100 mL of deionized water was used for NH$_3$ absorption, which was cooled with 5 °C circulated water by a chiller. It should be noted that the volume of the absorbing solution increased during electrolysis due to the condensation of water vapor and the decrease of solution density due to the increasing NH$_3$ content. For producing NH$_4$HCO$_3$, 100 mL of deionized water was pre-saturated with CO$_2$ and continuously bubbled with 500 mL min^{-1} of CO$_2$ during the electrolysis. Considering the decomposition temperature of NH$_4$HCO$_3$ (36 °C), the absorbing solution was also cooled with 5 °C circulated water and magnetically stirred at 400 r.p.m. Due to the relatively low solubility of NH$_4$HCO$_3$ (around 14.3 g in 100 mL of water), solid was precipitated in the absorbing solution. After the reaction, solid NH$_4$HCO$_3$ was obtained by vacuum filtration, followed by washing with ethanol and drying at room temperature. The remaining unabsorbed NH$_3$ from water and CO$_2$-saturated water was collected by a second absorbing solution containing 400 mL of 5 M H$_2$SO$_4$.

1.3 Direct NH$_3$ Fuel Cell Tests

The catalysts were deposited onto the electrode substrates by spray coating. For the preparation of the anode, a plain carbon cloth was first treated in HNO$_3$ (67–70%) at 110 °C for 1 h 45 min to improve its hydrophilicity. The catalyst ink was prepared by dispersing PtIr/C and AS-4 ionomer in 2-propanol (10 mg$_{catalyst}$ mL^{-1}), with a weight ratio of 9:1 between the catalyst and dry ionomer. The ink was then spray-coated onto the hydrophilic carbon cloth. For the cathode, the catalyst ink was prepared by dispersing Pt/C and AS-4 ionomer in a 7:3 mixture of 2-propanol and water (10 mg$_{catalyst}$ mL^{-1}), and the weight ratio between the catalyst and dry ionomer was 7:3, which was spray-coated onto a piece of carbon paper (Sigracet 22 BB). The final loading of platinum-group metal was 1.0 mg cm^{-2} for both cathode and anode.

NH$_3$ fuel cell tests were performed with a Scribner 850e Fuel Cell Test System. The fuel cell configuration includes stainless-steel end plates, gold-coated current collectors, graphite flow-field plates with serpentine channels, PTFE and silicone gaskets, two electrodes, and an anion-exchange membrane (Tokuyama A201). The active area of the membrane-electrode assembly (MEA) was 5 cm^2, which was formed after assembling the cell hardware. The cell temperature was 80 °C. 75 mL of the NH$_3$ solution obtained from MFAEL (with 1.25 M added KOH) was supplied to the anode and circulated by a peristaltic pump at a flow rate of 4 mL min^{-1}, and the reservoir of the NH$_3$ solution was kept at 5 °C by cooling water from a chiller. 500 mL min^{-1} of O$_2$ was passed through a humidifier at 80 °C before entering the cathode flow field at atmospheric pressure.

1.4 NO$_3^-$ Concentrating by Electrodialysis

1.4.1 The Electrodialysis System

The NO$_3^-$ concentrating experiment was conducted in a customized three-membrane and four-compartment electrodialysis cell on a flow-cell base apparatus (ElectroCell Inc.). The electrodialysis cell was constructed in the following configuration: "negative electrode | CEM | diluate solution | AEM | concentrate solution | CEM | positive electrode", where CEM and AEM stand for cation-exchange membrane and anion-exchange membrane, respectively. In this study, FKA-PK-130 (2.6 Ω cm^2 in Na$^+$) and FAA-PK-130 (2.2 Ω cm^2 in Cl$^-$) were used for CEM and

AEM, respectively, both from Fuma-Tech. A set of three rectangular sheets (2.5 cm × 2.0 cm) of stainless-steel meshes (80 × 80 mesh), was employed as the negative electrode, and a set of three rectangular sheets (2.5 cm × 2.0 cm) of Monel meshes (100 × 100 mesh) was employed as the positive electrode. A stainless-steel plate and a titanium plate were used as current collectors on the negative electrode and positive one, respectively. As defined by the single surface of one membrane in the electrodialysis pair "CEM | diluate solution | AEM | concentrate solution", the effective area of the electrodialysis pair was 5 cm^2 (2.5 cm in length and 2.0 cm in width). The compartment frames that enclose each of four compartment solutions in the electrodialysis cell were made of a high-performance fluorocarbon material (Viton) in 500 µm of thickness. A woven Nylon mesh (30 × 30 mesh) cut in the precise shape of flow channel was placed inside each compartment as the compartment spacer to hold the pace for fluid passing and to create the turbulence for fluid mixing.

Both diluate solution and concentrate solution have their own standalone storage containers: diluate container and concentrate container. The negative-electrode solution and the positive-electrode solution share the same electrode container. Two separate peristaltic pumps were utilized to control the flows of three solutions: one pump for both diluate solution and concentrate solution, and the other pump for the shared electrode solution. Four compartments of the electrodialysis cell are connected, through two peristaltic pumps, with three solutions by 1/8" tubing (Masterflex® Precision L/S-16).

1.4.2 Electrodialysis Operation

The electrodialysis operation was carried out by applying a constant current (*e.g.*, 1 mA cm^{-2}) using a potentiostat/galvanostat (VersaSTAT 3F, AMETEK) between the negative electrode and the positive electrode of the electrodialysis cell for a certain time matching the designed the NO_3^- removal (75%) from the diluate solution. During the electrodialysis operation, the voltage of the cell was measured and recorded as the voltage profile of the three-membrane electrodialysis. 7.14 mM KNO_3, equivalent to 100 ppm NO_3^--N, was used as the initial diluate solution; 2 M KNO_3 (28,000 ppm NO_3^--N) was used as the concentrate solution; and 2 M KCl was used as the electrode solution for both negative electrode and positive one. Note that a large amount of concentrate solution was used, and therefore, its concentration (2 M KNO_3) was practically treated as a constant (<0.05% of change) during the electrodialysis operation. In this study, a constant flow rate of 60 mL min^{-1} was precisely controlled for each of the four compartments, leading to 10 cm s^{-1} of the nominal fluid velocity through each of the four compartments. Prior to use, both FKA-PK-130 and FAA-PK-130 membranes were treated with 0.5 M KCl for 48 h. Distilled water was used to prepare all solutions in this study.

After the electrodialysis operation, the NO_3^- concentration of the finial diluate solution was analyzed (detailed in 1.5.2). The detected concentration of the remaining NO_3^- in the diluate solution after electrodialysis operation was 1.99 mM, corresponding to 96.3% of coulombic efficiency: $(7.14 - 1.99)$ mM / $(7.14$ mM × 75% of designed NO_3^- removal).

1.4.3 Voltage Profile of the Electrodialysis Pair

The voltage profile of the electrodialysis pair was obtained by subtracting the voltage profile of single-membrane background cell from that of three-membrane electrodialysis. The single-membrane background cell was constructed by assembling the negative electrode, one CEM, and the positive electrode, configured as "negative electrode | CEM | positive electrode". Clearly, the cell voltage of this single-membrane cell consists of the sum of the background voltage losses

including ohmic loss from one CEM and the two electrode compartments, electron-transfer kinetic loss from both electrodes, and mass-transport loss from the two electrode solutions.

Because of the required electron transfer, electrochemical reactions do occur on the electrodes of the electrodialysis cell: hydrogen evolution and/or oxygen reduction take place on the negative electrode; and oxygen evolution and/or hydrogen oxidation take place, depending on the scale of current density and electrolyte conditions. No specific electrocatalyst was applied on either of the two electrodes, and thus the kinetic overpotentials were often considerable. Nevertheless, the background cell is exactly shared with the electrodialysis cell, and therefore, the voltage of the electrodialysis pair, by comparing the three-membrane electrodialysis cell and the single-membrane background cell, reflects the true electrodialysis behavior.[3] Considering that practical electrodialysis systems comprise a few hundred electrodialysis pairs with only one set of background cell (the negative electrode, one CEM, and the positive electrode), the voltage from the background cell is usually insignificant compared with the voltage from those electrodialysis pairs.

1.5 Product Quantification

1.5.1 Quantification of NH_3

NH_3 in the absorbing solution (0.1 M H_2SO_4) was quantified by the indophenol blue colorimetric method. Four freshly prepared reagents were used, including (a) coloring solution, containing 0.4 M sodium salicylate and 0.32 M NaOH; (b) oxidizing solution, containing 0.75 M NaOH in NaClO solution; (c) catalyst solution, containing 10 mg ml^{-1} of $Na_2[Fe(CN)_5NO]\cdot 2H_2O$; and (d) 6 M NaOH solution. The sample solution was first diluted with 0.1 M H_2SO_4 to the proper range of NH_3 concentration. 4 mL of the diluted sample solution was then added into a glass vial, followed by the sequential addition of 200 μL of (d), 50 μL of (b), 500 μL of (a), and 50 μL of (c). The reagents were mixed by shaking vigorously and kept in a dark place for color development. After 2 h, absorbance was measured by a UV-Vis spectrophotometer (Shimadzu UV-2700) at 660 nm. The calibration curve was established by testing a series of standard NH_3 solutions ranging from 0 to 2.5 mg L^{-1} (in NH_3-N) diluted with 0.1 M H_2SO_4.

For the ^{15}N isotope labeling experiment, the concentrations of $^{14}NH_3$ and $^{15}NH_3$ (in 0.1 M H_2SO_4) were determined by ^1H Nuclear Magnetic Resonance (NMR) spectroscopy on an NMR spectrometer (Bruker Avance NEO 400 MHz). The sample solution was first diluted with 0.1 M H_2SO_4 to the proper range of NH_3 concentration. 800 μL of the diluted sample solution was then mixed with 200 μL of DMSO-d_6 and 200 μL of 32 μM maleic acid in DMSO-d_6 (internal standard). The scan number was 1,024 with a water suppression method. Standard $^{14}NH_3$ and $^{15}NH_3$ solutions were prepared for calibration with concentrations ranging from 0 to 5 mg L^{-1} (in ^{14}N and ^{15}N). NH_3 content in CO_2-saturated water was also quantified by ^1H NMR due to the pH-sensitive nature of the colorimetric method.

Ion chromatography (IC) was also employed for NH_3 quantification to verify the accuracy. IC measurements were performed on a Dionex™ Easion system equipped with a conductivity detector, 4 mm Dionex IonPac CG12A/CS12A columns, and a CCRS 500 suppressor. The mobile phase was 20 mM methanesulfonic acid, and was pumped at a flow rate of 1.0 mL min^{-1}. The running time was 8 min. The calibration solutions were prepared with $(NH_4)_2SO_4$ in the concentration range of 20–100 mg L^{-1} (in NH_3-N).

1.5.2 Quantification of NO_3^- and NO_2^-

NO$_3^-$ and NO$_2^-$ in the diluted electrolyte were analyzed by High-Performance Liquid Chromatography (HPLC)[4] (Agilent Technologies, 260 Infinity II LC System) equipped with a variable wavelength detector (Agilent 1260 Infinity Variable Wavelength Detector VL). The wavelength of 213 nm was chosen for NO$_3^-$ detection. A C18 HPLC column (Gemini® 3 μm, 110 Å, 100 × 3 mm) was used for analysis at 25 °C with a binary gradient pumping method to drive the mobile phase at 0.4 mL min^{-1}. The mobile phase consisted of 0.01 M *n*-Octylamine in a mixed solution containing 30 vol.% methanol and 70 vol.% deionized water, and the pH of the mobile phase was adjusted to 7.0 with phosphoric acid. The running time was 30 min. The calibration solutions for NO$_3^-$ or NO$_2^-$ were prepared with KNO$_3$ or KNO$_2$ in the concentration range of 0.0625–2 mM.

1.5.3 Identification and Quantification of Organic Products

To identify the products from the oxidation of C–N bonds, we used ^{13}C-labeled glycine and alanine as simple organic Nr compounds as the reactants in MFAEL, and analyzed the products by ^{13}C NMR on an NMR spectrometer (Bruker Avance NEO 400 MHz). 1 mL of the sample solution (diluted electrolyte) was mixed with 200 μL of D$_2$O and 200 μL of 50 mg mL^{-1} DSS solution (internal standard). The scan number was 128.

To quantify the reactant (alanine) and product (acetate) after electrolysis, ^{1}H NMR was carried out on a Bruker AVIII-600 MHz NMR spectrometer. 400 μL of the sample solution (diluted electrolyte) was mixed with 200 μL of D$_2$O and 100 μL of 15 mM dimethylmalonic acid (DMMA) solution (internal standard). The scan number was 8. The calibration solutions for alanine and acetate were prepared in the concentration range of 0–20 mM.

The carboxylic acid products were also identified and quantified by HPLC. The wavelength of 220 nm was selected. An OA-1000 organic acids column (Grace®, length: 300 mm, ID: 6.5 mm, part no. 9046) was used for analysis at 25 °C with a binary gradient pumping method to drive the mobile phase (5 mM sulfuric acid) at 0.6 mL min^{-1}. The running time was 30 min. Solutions prepared by a series of standard chemicals were also tested by ^{13}C NMR and HPLC for product identification, including carbonate, formate, glycolate, glyoxylate, oxamate, oxalate, lactate, pyruvate, acetate, and acrylate.

1.5.4 Quantification of Gaseous Products

The gaseous products of NO3RR in the NaOH/KOH/H$_2$O electrolyte were analyzed by online gas chromatography (SRI Instruments, 8610C, Multiple Gas #3) equipped with HayeSep D and MolSieve 5Å columns and a thermal conductivity detector. The MFAEL was operated under the same conditions specified in 1.2.1, except that Ar or He was used as the carrier gas at a lower total flow rate of 85 mL min^{-1}. The same carrier gas was used for the MFAEL and GC. During the measurement with Ar, a 8-min programmed cycle was repeated, including 6 min of the GC running period and 2 min of the cooling period. During the measurement with He, a 16-min programmed cycle was repeated, including 11 min of the GC running period and 5 min of the cooling period.

For each cycle, the generation of product i (n_i, mol) was calculated by

$$n_i = c_i \times 10^{-6} \times \frac{p\dot{V} \times 10^{-6} \times t}{RT}$$

where c_i is the concentration (ppmv) of product i; $\dot{V}$ is the volumetric flow rate of the gas (mL min^{-1}); p is the atmospheric pressure ($p = 1.013 \times 10^5$ Pa); R is the gas constant ($R = 8.314$ J mol^{-1} K^{-1}); T is the room temperature (293.15 K); t is the running time of each cycle (min). The

calibration curves of H_2 (10–10,000 ppm) and N_2 (100–100,000 ppm) were established by analyzing the standard calibration gases.

1.6 Physical Characterization

X-Ray Diffraction (XRD) crystallography was carried out on a Rigaku Smartlab high-resolution X-ray diffractometer with Cu K-alpha radiation (wavelength, λ = 1.5406 Å) and a tube voltage of 40 kV (with a tube current of 30 mA). The scan was performed at a rate of 10° min^{-1} and a step size of 0.01°. Scanning electron microscopy (SEM) imaging and Energy Dispersive X-ray Spectroscopy (EDS) were performed on a FEI Quanta-250 field-emission scanning electron microscope with a light-element X-ray detector and an Oxford Aztec energy-dispersive X-ray analysis system. X-ray Photoelectron Spectroscopy (XPS) was performed on a Kratos Amicus/ESCA 3400 X-ray photoelectron spectrometer with Mg K-alpha X-ray (1,253.7 eV), and all spectra were calibrated with the C 1s peak at 284.8 eV. Raman spectra were collected using an inVia 488 nm Renishaw Coherent Laser Raman Spectrometer calibrated to an internal standard silicon reference centered at 520.5 ± 0.5 cm^{-1}. Samples were tested under a 20x objective lens, with a spot size of ~2500 μm^2, from 100–4000 cm^{-1} with 10 accumulations at 12.5 mW power.

2. Techno-Economic Analysis (TEA)

2.1 TEA of NO_3^- Concentrating by Electrodialysis

The techno-economic analysis (TEA) was conducted to evaluate the levelized total cost (LTC) of NO_3^- concentrating by electrodialysis, on account of the unit kmol-NO_3^- recovered from NO_3^--containing wastewater. As the two major constituents of the LTC (*i.e.*, LTC = LCC + OPEX), the levelized capital cost (LCC) and the operational expense (OPEX) were synergistically analyzed by sharing the key parameters. For example, the dimensions of the electrodialysis stack were the input for optimizing OPEX (by fluid velocity) as well as finding operational current density. The operational current density determined the total required area of electrodialysis pair per unit of kmol-NO_3^- and thus the corresponding capital cost. The hierarchical structure of the TEA in this study is presented in Fig. S27. The detailed TEA assumptions and results are shown in Fig. S28.

Capital cost analysis was performed by virtue of a typical medium-size commercial electrodialysis stack: 40 cm × 160 cm for each electrodialysis pair, and 250 pairs in total. The market price of the electrodialysis system is \$35,000 (Hangzhou Iontech Environmental Tech Co. Ltd.). The LCC was calculated via the standard capital recovery method on the following assumptions: 40 years of service time,[5] 19% as the cost ratio of maintenance to the system, 3% of annual discount rate,[6] 83.3% of capacity factor (300 days per year for operation), and 90% of coulombic efficiency.

Energy consumption was considered to be the sole source for the OPEX, with three following contributors to energy consumption: electrodialysis (by analyzing pair voltage, operational current, and efficiencies), pumping (by analyzing pair pressure drop, flow rate, and efficiencies), and others (by assuming 10% of the sum of the first two sources).

Unless otherwise specified, the following set of design and operational parameters was employed for analyzing the OPEX: 7.14 mM $NaNO_3$ (100 ppm NO_3^--N) as the initial diluate solution (C_s); 2 M $NaNO_3$ (28,000 ppm NO_3^--N) as the initial concentrate solution (C_c); 2 M $NaNO_3$ as the electrode solution (C_e); 0.05 mm as the intermembrane distance in an electrodialysis pair (d); 4 cm s^{-1} as the nominal fluid velocity; \$0.07 kWh^{-1} as the electricity price; 80% as the designed NO_3^- recovery from diluate NO_3^-. The electrodialysis pair in this work comprises one anion-exchange membrane (assuming 2.5 Ω cm^2, such as FAA-PK-130, Fuma-Tech, 2.2 Ω cm^2 in Cl^- or 2.35 Ωcm^2 in NO_3^-), one cation-exchange membrane (assuming 2.5 Ω cm^2, such as FKA-PK-130, Fuma-Tech, 2.6 Ω cm^2 in Na^+), one compartment of diluate solution (0.05 cm thick, 100 ppm NO_3^--N or 7.14 mM $NaNO_3$, with a porous Nylon mesh as the spacer), and one compartment of concentrate solution (0.05 cm thick, 2 M $NaNO_3$, with a porous Nylon mesh as the spacer).

The limiting current density depends heavily on species conditions (concentration and diffusion coefficient), operational conditions (fluid velocity), and geometric dimensions/locations (pair distance and flow length). In this study, limiting current density was calculated by adopting the classic Rosenberg and Tirrell equation,[7] and considering the hydraulic diameter in the presence of spacer.[8] Pressure drop through electrodialysis pair is calculated by the Darcy-Weisbach equation with a modified channel hydraulic diameter.[8] The total pressure drop was obtained by using 0.5 as the ratio of the pair pressure drop to the total pressure drop.[9] Other minor assumptions were also taken, including 90% of limiting current density used as the operating current density,[10] 90% of voltage efficiency, 90% of coulombic efficiency, and 80% of pumping efficiency.

The readers should note that the presence of spectator anions (SO_4^{2-} and Cl^-) in real-world wastewater will lower the current efficiency, but reduce the required pair voltage (through raising

ionic conductivity). The exact impact of those spectator anions on energy consumption and cost estimation will depend largely on a variety of preconditions including the concentration ratio of spectator anions to NO_3^-, the composition of spectator anions, and the ionic selectivity against NO_3^- across the anion-exchange membrane. None of those preconditions is well established or widely accepted for NO_3^--containing wastewater, and therefore the impact of spectator anions is not factored here in this work. For specific wastewater, the spectator anions should be considered for more accurate cost estimation.

2.2 TEA of NO_3^--to-NH_3 Conversion by Electrolysis in MFAEL

The TEA was performed for the NO_3^--to-NH_3 conversion by electrolysis in MFAEL on account of the unit kmol-NH_3 produced from NO_3^- by electrolysis. LCC, OPEX, and then LTC were synergistically analyzed by sharing the key parameters. The hierarchical structure of the TEA in this study is presented in Fig. S30. The detailed TEA assumptions and results are shown in Fig. S31.

Unless otherwise specified, the following set of design and operational parameters was employed: 120 °C as cell temperature, NaOH/KOH/H_2O with 40 wt.% water content and equal molar NaOH and KOH as the electrolyte, 250 mA cm^{-2} as current density, 2.7 V as cell voltage, 90% of faradaic efficiency for NO_3^--to-NH_3 conversion, \$0.07 kWh^{-1} as electricity price, and 83.3% of capacity factor (300 days per year for operation).

Energy consumption was also considered to be the sole source of the OPEX. In addition to electrolysis energy consumption, both heating energy consumption and mixing energy consumption were considered. Mixing energy consumption was analyzed by the McCabe and Smith method,[11] while the heating energy consumption was assumed as 5% of electrolysis energy consumption. Both density and viscosity of NaOH/KOH/H_2O electrolyte as functions of temperature were taken into account in light of Asdrubali's work.[12]

Capital cost analysis was performed based on a medium-size MFAEL stack with 100-L electrolyte capacity (50 cm × 50 cm × 40 cm). The electrodes were extended by 12 fins in total, with 2,800 cm^2 of surface area per fin (40 cm × 35 cm per × 2 sides), totaling the electrode area of 3.36 m^2. Specifically, the capital cost of manufacturing such 100-L MFAEL was obtained by first summing a) material costs, including all key components: cathode materials (nickel mesh), anode materials (nickel mesh), electrolyte constituents (NaOH and KOH), and cell body materials (PTFE as liner and stainless steel as shell); and then b) all major ancillary and auxiliary parts, including stirring motor/parts, gaskets, current collectors, power electronics, combined heat and power unit, and temperature conditioning. The cost of all identified materials/parts was found to be \$1,164 per system. The cost of all unidentified parts was assumed as 10% of that of all identified parts/materials. Then, 10% of cost contingency, 50% of sales markup, and 70% of system installation were added on top of the cost of all identified and unidentified parts/materials.[13] The total capital expense (CAPEX) of such electrolyzer was found to be \$3,121 per system.

By means of the standard capital recovery method, the LCC for NO3RR associated with the total capital cost of \$3,121 per system was calculated to be \$0.97 per kmol-NH_3, on the following set of assumptions: 20 years of service time, 19% as the cost ratio of maintenance to the system (assumed to be the same as that of electrodialysis), 3% of annual discount rate,[6] 83.3% of capacity factor (300 days per year for operation), and 90% of coulombic efficiency.
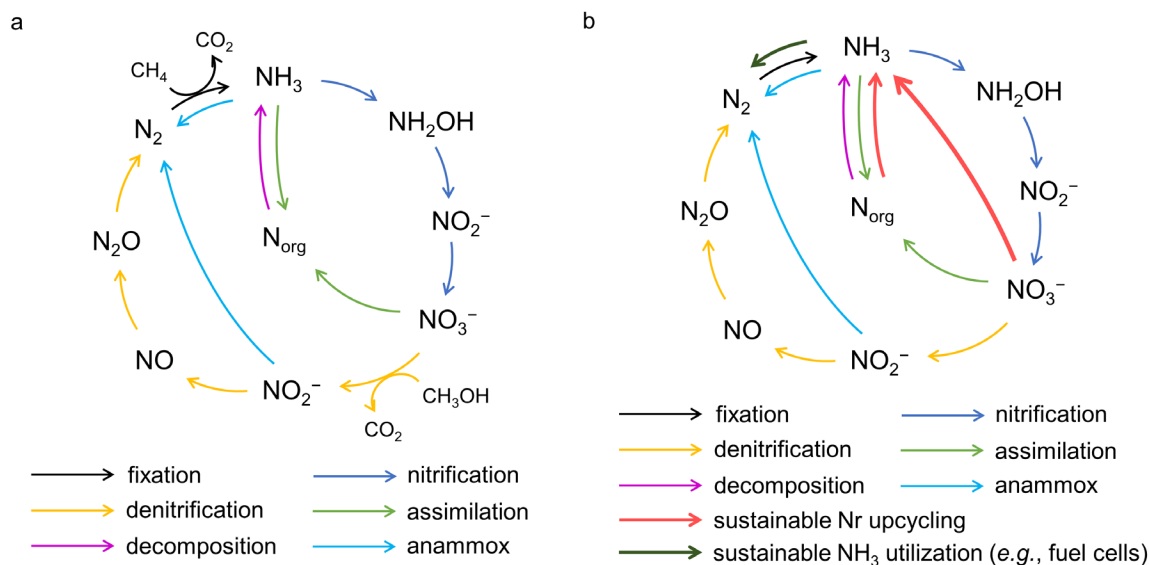
3. Supplementary Figures (S1–S41)

Fig. S1. A simplified representation of the N cycle. (a) The current N cycle with a growing imbalance between N_2 and Nr. (b) The proposed future NH_3-centric N cycle with enhanced Nr recycling, in which the NH_3 demand can be largely fulfilled by the conversion of existing Nr instead of the fixation of N_2. Through its utilization as an energy carrier (*e.g.*, in fuel cells), NH_3 can be converted back to N_2, closing the N cycle. Abbreviations: N_{org}, organic Nr compounds. Note that the anthropological N_2 fixation and denitrification processes are both accompanied by the unavoidable emission of considerable greenhouse gases: each N atom fixed by the Haber-Bosch process results in the generation of 0.375 CO_2 molecules (from the steam reforming reactions); each NO_3^--N atom requires 0.83 molecules of CO_2 to be fully denitrified to the harmless N_2 (assuming methanol as the carbon source). By switching toward the renewable NH_3-centric N cycle, these CO_2 emissions should be largely mitigated.
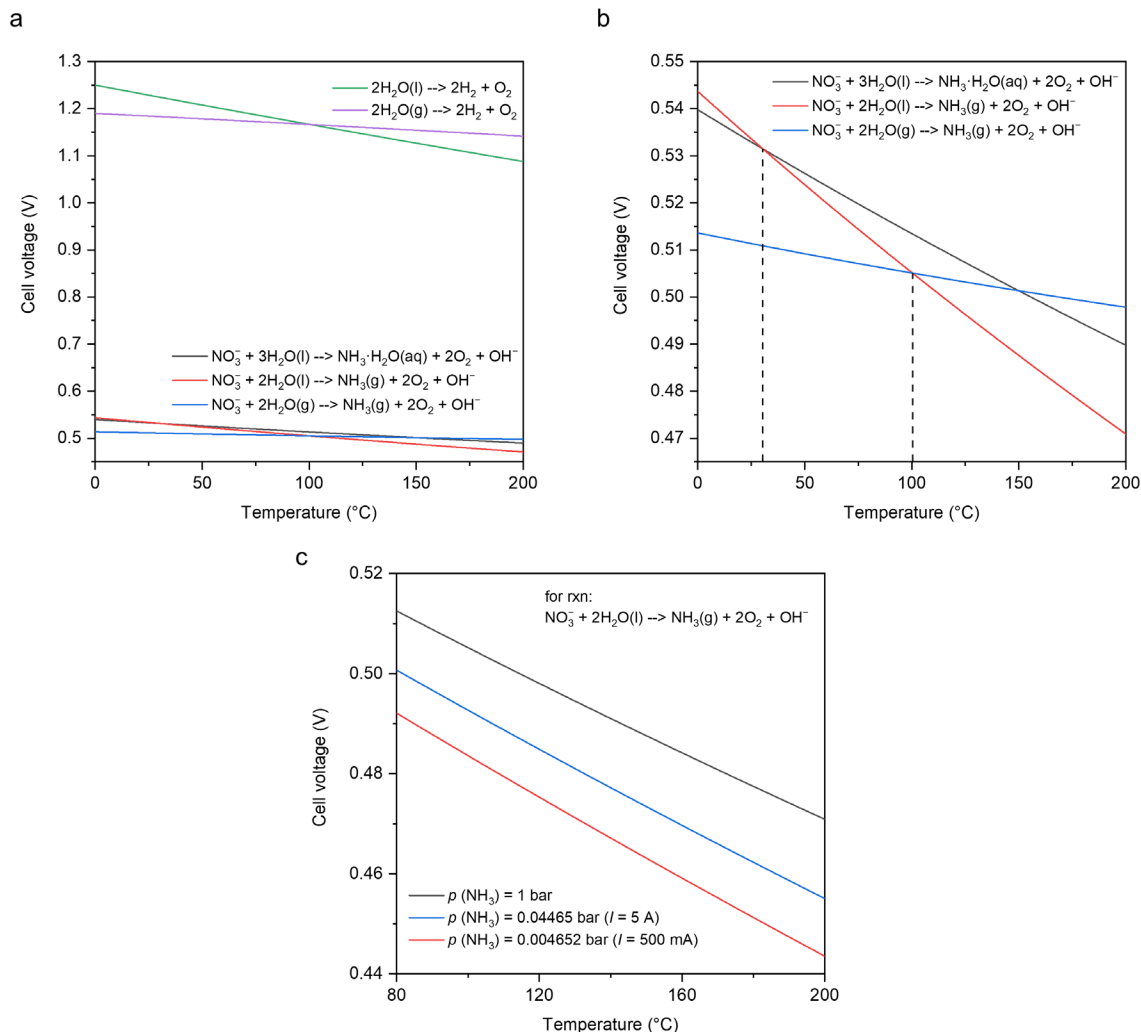
Fig. S2. Thermodynamic calculations of NO3RR and hydrogen evolution reaction (HER) paired with oxygen evolution reaction (OER). All thermodynamic parameters were obtained from Ref. [14] (a) Dependence of thermodynamic cell voltage on temperature for different reactions, considering liquid (l) or gaseous (g) H_2O as the reactant, and aqueous (aq) or gaseous (g) NH_3 as the product. (b) Zoom-in view of (a) for NO3RR. (c) Comparison of thermodynamic cell voltage at different NH_3 partial pressures. 0.04465 and 0.004652 bar corresponds to the NH_3 partial pressure in MFAEL operated at 5 A and 500 mA, respectively, assuming 200 mL min^{-1} of the carrier gas flow rate and 100% faradaic efficiency towards NH_3. Note: the calculations show that NO3RR is much more favorable than HER under alkaline conditions, and the cell voltage decreases with increasing temperature. At temperature higher than 30 °C, producing gaseous NH_3 is thermodynamically more favorable than aqueous NH_3. Liquid-phase H_2O as the reactant is thermodynamically more favorable than gaseous H_2O. Using a carrier gas to remove the produced NH_3 can shift the chemical equilibrium and thus make the reaction more thermodynamically favorable. These calculations justify our choice of reaction conditions in MFAEL: strong alkalinity to suppress HER; mildly elevated temperature with a continuous flow of carrier gas for the rapid evolution of gaseous NH_3; liquid water (40 wt.%) preserved in the electrolyte as the reactant.
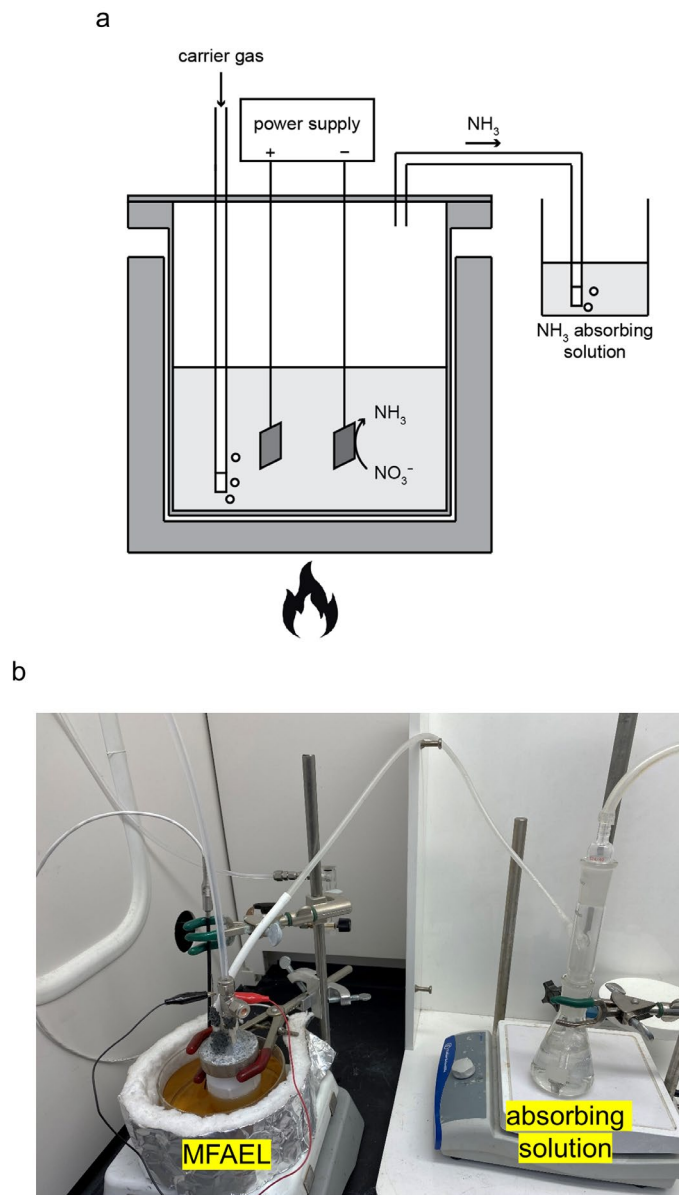
13

a

b

Fig. S3. The MFAEL system for NO3RR. (a) Schematic diagram and (b) photo of the MFAEL system.
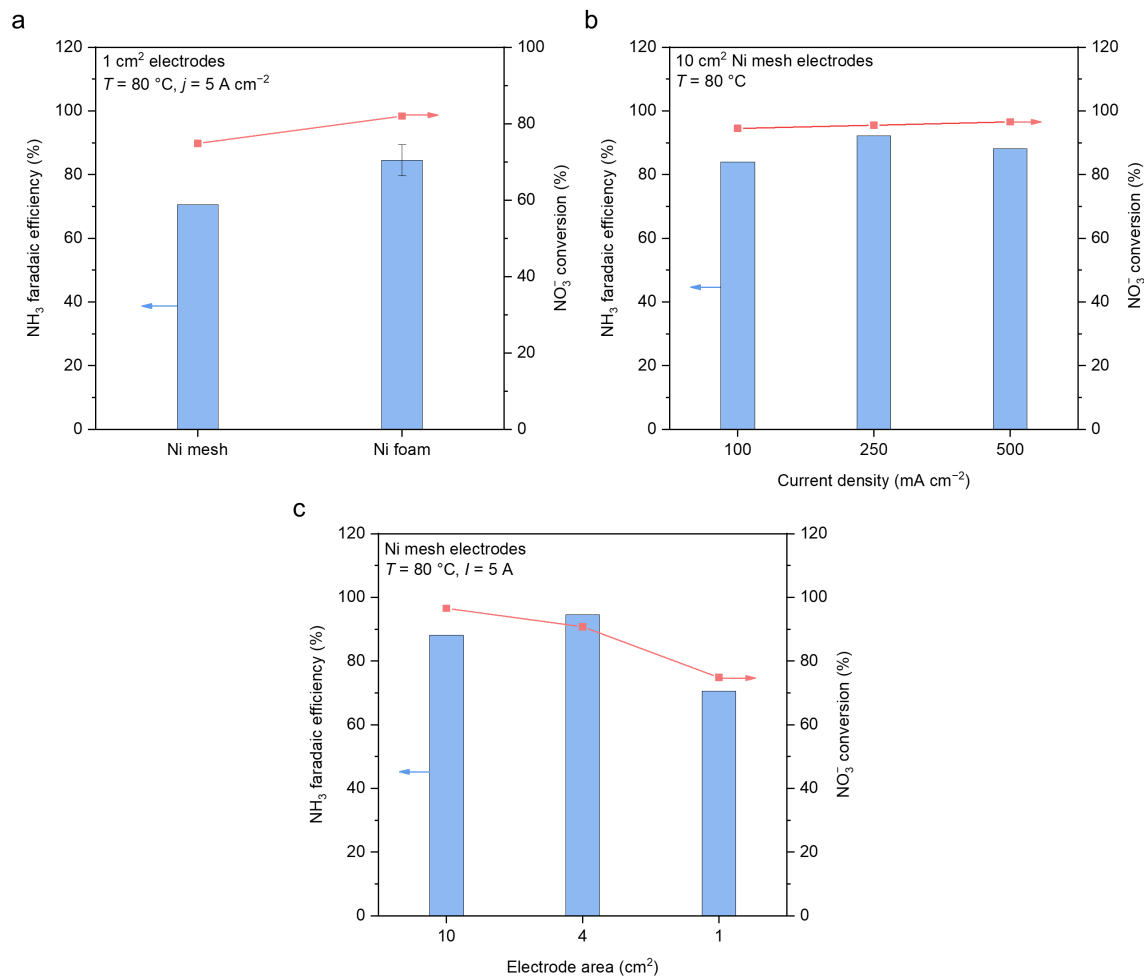
14

Fig. S4. NO3RR in the NaOH/KOH/H$_2$O electrolyte at varying current densities on Ni-based electrodes. The left and right y-axis show the faradaic efficiency of NH$_3$ and the conversion of NO$_3^-$, respectively. For all measurements, the amount of added KNO$_3$ was equal to the theoretical amount of NO$_3^-$ that can be fully converted to NH$_3$ based on the applied charge. (a) Comparison of NO3RR performance using two identical Ni mesh and Ni foam as electrodes at 5 A cm^{-2}. The geometric area of the electrodes was 1 cm^2. (b) NO3RR performance for current densities in the range of 100–500 mA cm^{-2}. (c) NO3RR performance with 5 A of applied current with different areas of the Ni mesh electrodes. The same electrode area was used for both cathode and anode.
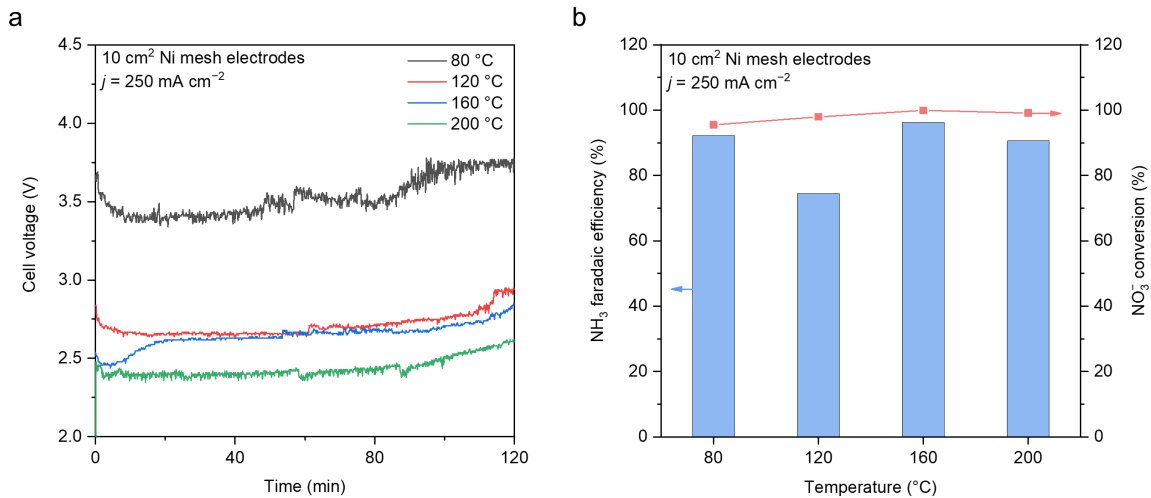
Fig. S5. NO3RR in the NaOH/KOH/H₂O electrolyte at temperatures ranging from 80 to 200 °C. (a) Cell voltage profiles of the 2-hour constant-current electrolysis for NO3RR at 250 mA cm⁻². (b) The corresponding faradaic efficiency of NH₃ and the conversion of NO₃⁻.
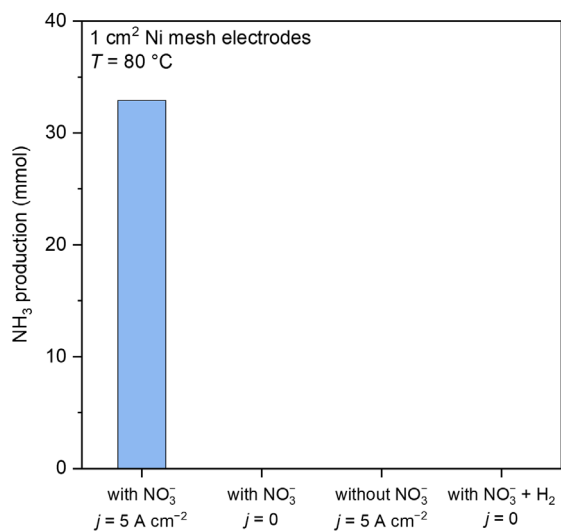
Fig. S6. Control experiments of NO3RR in the NaOH/KOH/H$_2$O electrolyte. From left to right: 1st column, with 46.64 mmol of added KNO$_3$ and 5 A cm^{-2} of applied current density. 2nd column, with 46.64 mmol of added KNO$_3$ and no applied current. 3rd column, with 5 A cm^{-2} of applied current density and no added KNO$_3$. 4th column, with 46.64 mmol of added KNO$_3$ and 200 mL min^{-1} of H$_2$ feed, and no applied current. The reaction time was 2 h for all 4 experiments.
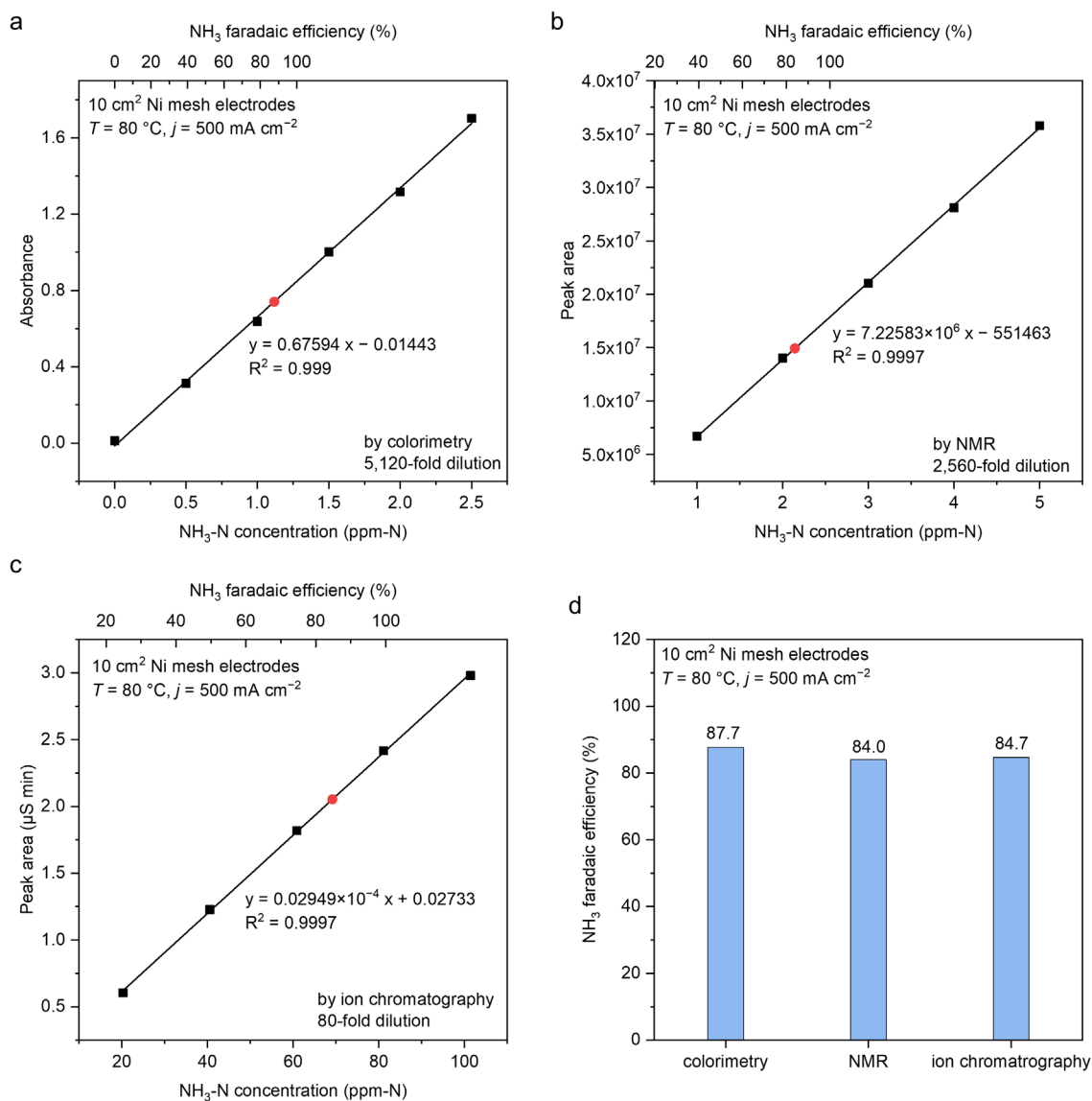
Fig. S7. Comparison of the results of NH_3 quantification by different methods: (a) indophenol colorimetry, (b) ^{1}H NMR, and (c) ion chromatography. The black squares represent the calibration solutions, and the red circles represent the sample solution. The sample solution was obtained from NO3RR in the $NaOH/KOH/H_2O$ electrolyte at 5 A (500 mA cm^{-2}) for 2 hours. Note that the 3 methods require different folds of dilution to satisfy their measurement ranges (colorimetry: 5,120-fold; ^{1}H NMR: 2,560-fold; ion chromatography: 80-fold). (d) Comparison of the calculated FE towards NH_3 determined by different methods.

18
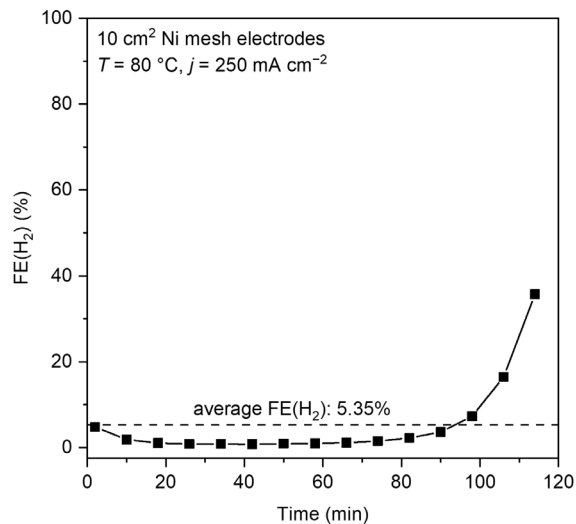
Fig. S8. Faradaic efficiency of H_2 for NO3RR in the NaOH/KOH/H_2O electrolyte at 250 mA cm^{-2} determined by online GC. Note: the average FE towards H_2 during 2-hour NO3RR electrolysis was 5.35%. This agrees well with the high FE towards NH_3 (92.2%) under this condition, suggesting that HER in the NaOH/KOH/H_2O electrolyte is largely suppressed in the presence of NO_3^-. FE towards H_2 decreased in the initial period of electrolysis, which could be due to the formation of nanostructured Ni on the cathode. The increase in FE(H_2) after 80 min is because of the consumption of NO_3^- (the overall NO_3^- conversion was 95.5%).

19

Fig. S9. NH$_3$ FE and NO$_3^-$ conversion of NO3RR in the NaOH/KOH/H$_2$O electrolyte at 500 mA cm^{-2} with different carrier gases. Air was pre-scrubbed in 0.1 M KOH to remove trace CO$_2$ before entering the MFAEL.
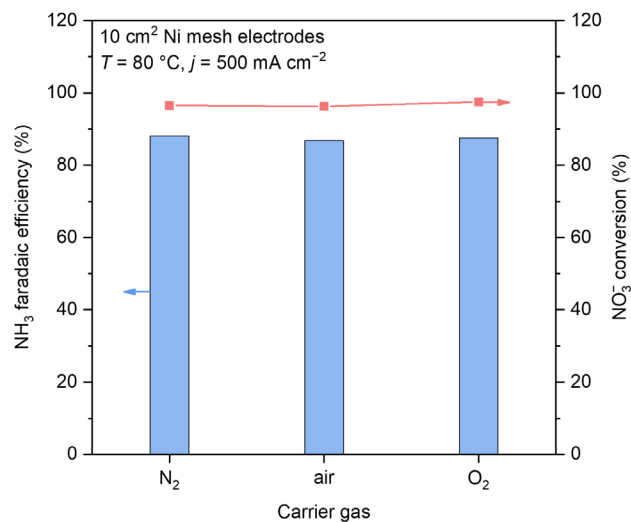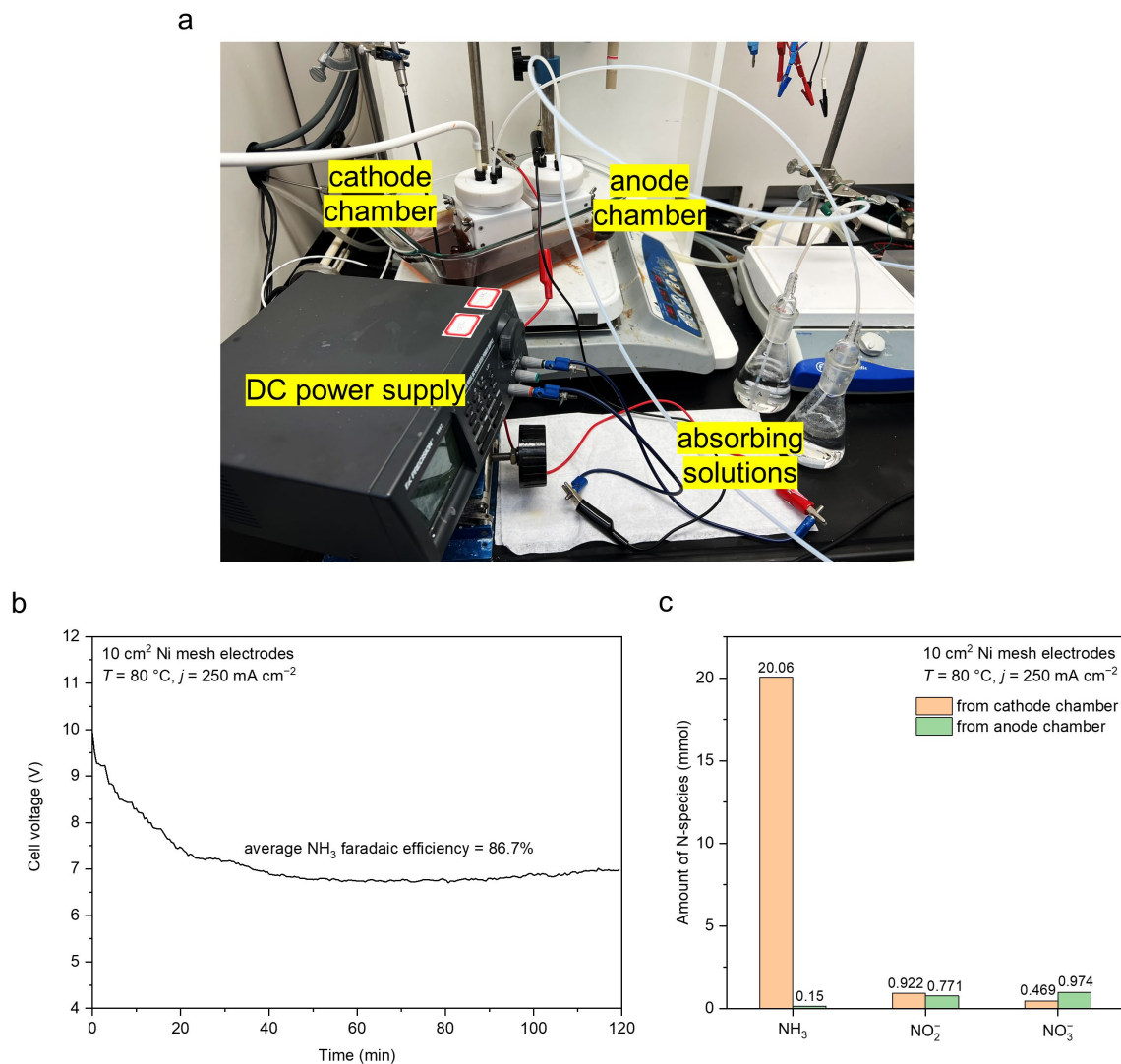
Fig. S10. NO3RR in a divided H-type cell system. The cathode and anode chambers were separated by a PTFE mesh (0.025" × 0.005" opening) to prevent the gas crossover. KNO_3 was initially added to the cathode chamber, and electrolytes in both chambers were bubbled with 100 mL min^{-1} of N_2 as the carrier gas into two separate H_2SO_4 absorbing solutions; other operating conditions were kept the same as the undivided MFAEL reactor. (a) Photo of the divided cell system. (b) Cell voltage profiles of the 2-hour constant-current electrolysis at 250 mA cm^{-2}. (c) Distribution of the reactant and products from the cathode and anode chambers. Note: at 250 mA cm^{-2}, the divided cell that is free of gas crossover produced NH_3 at the same level of high FE (86.7%) as the undivided MFAEL reactor (92.2%). The cell voltage was higher compared to the undivided reactor due to the separator and the larger distance between the electrodes. The vast majority of produced NH_3 was collected from the cathode side, suggesting the rapid evolution of NH_3 from the NaOH/KOH/H_2O electrolyte.
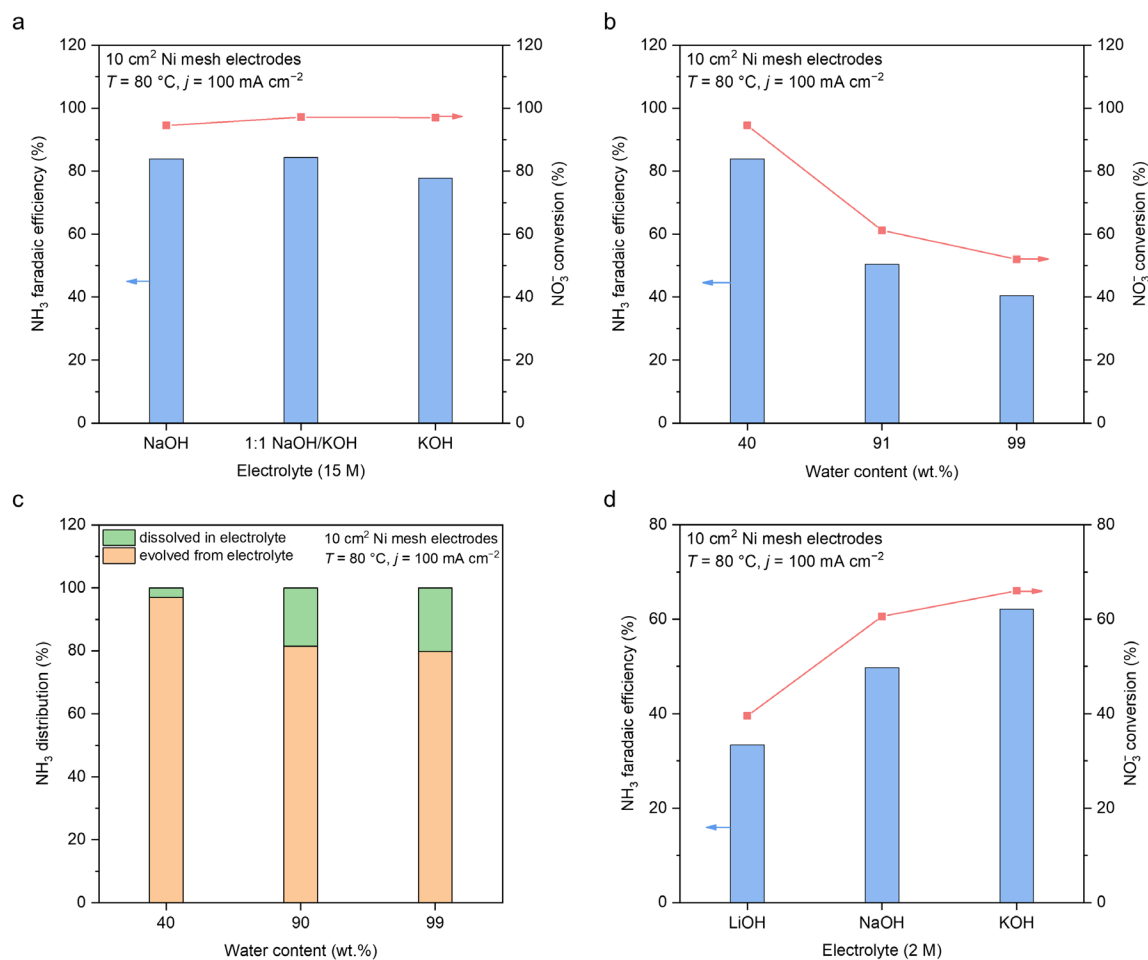
Fig. S11. Effect of electrolyte composition on the NO3RR performance in MFAEL. For the ternary NaOH/KOH/H$_2$O electrolyte, 40, 91, and 99 wt.% of water correspond to 15, 2 M, and 0.2 M OH$^-$, respectively. (a) Comparison of NO3RR performance at 100 mA cm^{-2} in the ternary electrolyte (NaOH/KOH/H$_2$O with 1:1 molar NaOH/KOH) and binary electrolytes (NaOH/H$_2$O and KOH/H$_2$O). The OH$^-$ concentration was 15 M for the ternary and binary electrolytes. (b) Comparison of NO3RR performance in the ternary NaOH/KOH/H$_2$O electrolyte with different alkalinity. (c) Distribution of produced NH$_3$ in the MFAEL systems with different alkalinity after 2-hour electrolysis. The orange and green portions of the columns show the percentage of NH$_3$ detected in the absorbing solution and the electrolyte, respectively. (d) NO3RR in the 2 M electrolyte with different alkalis. Note: with increased water content, more NH$_3$ was retained in the electrolyte instead of being carried out by the flow of carrier gas. In our measurements, we kept the system with gas bubbling for an additional 30-minute period after electrolysis, which was found to be sufficient to deplete the remaining NH$_3$ in the electrolyte with 40 wt.% of water.

22

Fig. S12. SEM images of Ni mesh electrodes. (a) Bare Ni mesh before electrolysis. (b) Ni mesh cathode and (c) anode after NO3RR measurement in the NaOH/KOH/H_2O electrolyte at 5 A cm^{-2}. (d)–(f) The corresponding images of (a)–(c) at higher magnification. Note: from the SEM images, no considerable structural change was observed for the anode after electrolysis in the NaOH/KOH/H_2O electrolyte. The cathode surface shows some nanostructured features, which is a combination of ~100 nm particles and hexagonal flakes with a diameter of 1–2.5 μm.
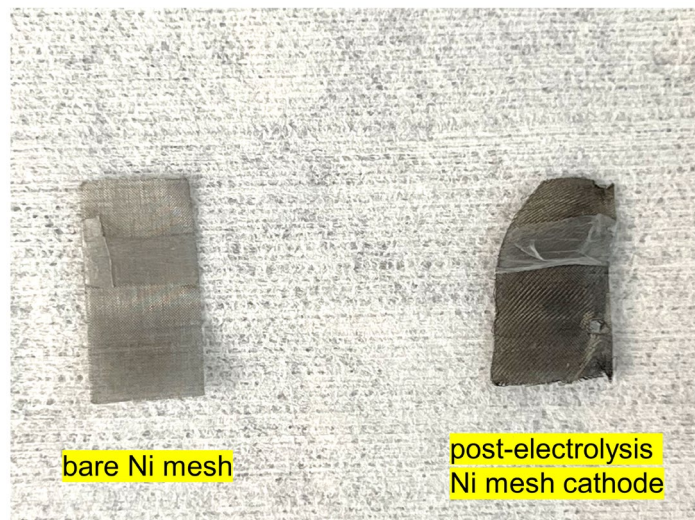
Fig. S13. Photo of the bare Ni mesh electrode (left) and the post-electrolysis Ni mesh cathode (right).

Sample	Ni (at.%)	O (at.%)	C (at.%)	Si (at.%)
bare Ni mesh	86.13	1.22	12.45	0.20
post-electrolysis Ni mesh cathode (sum)	61.02	24.34	12.47	2.17
post-electrolysis Ni mesh cathode (area 1)	67.08	18.33	12.97	1.63
post-electrolysis Ni mesh cathode (area 2)	34.13	47.40	15.81	2.66
post-electrolysis Ni mesh anode	84.44	3.91	11.08	0.58
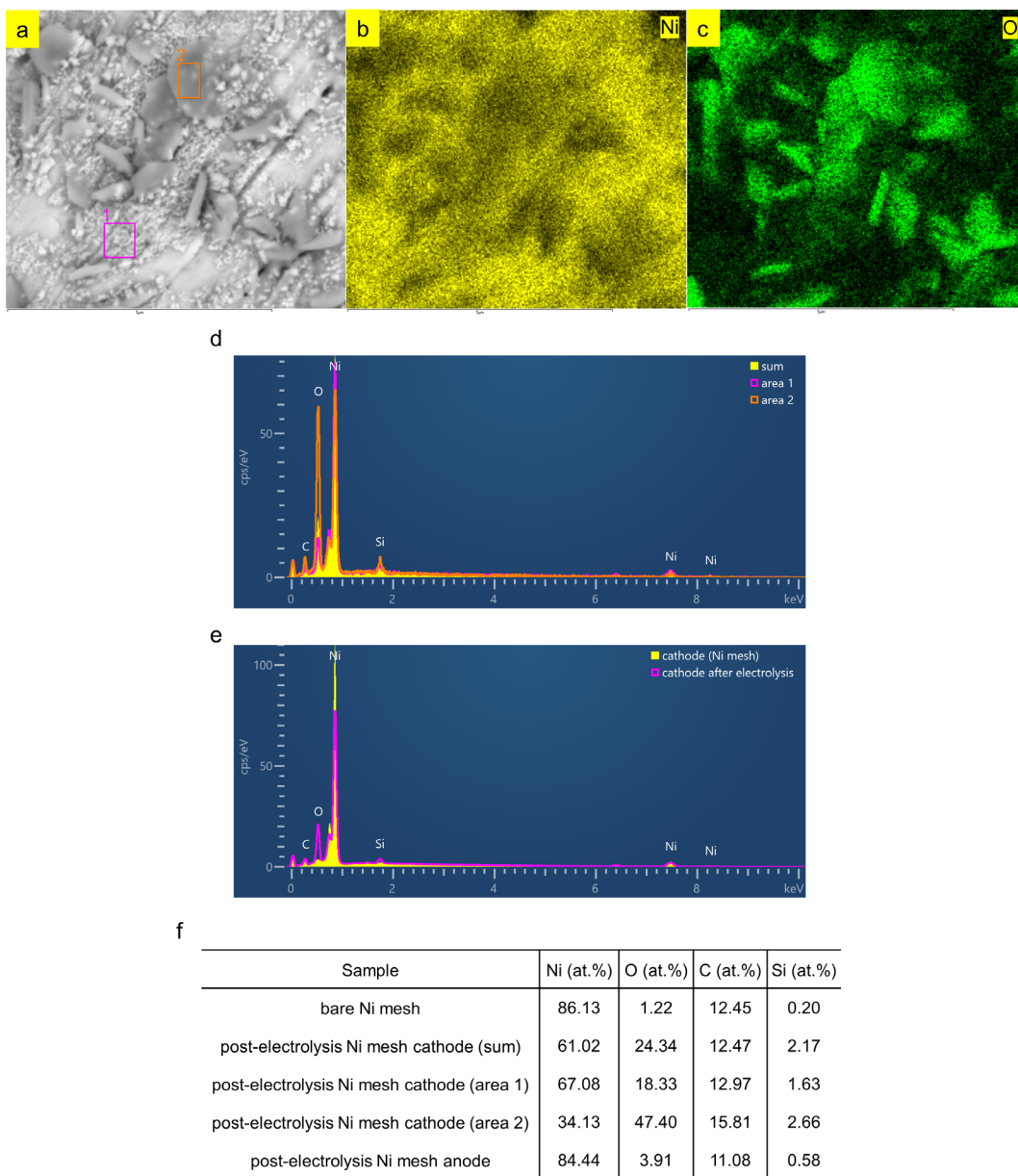
Fig. S14. SEM-EDS analysis of Ni mesh electrodes. (a) SEM image of the post-electrolysis Ni mesh cathode. (b)–(c) The corresponding elemental mappings of Ni and O. (d) EDS of the entire region (sum) and two selected areas of (a). (e) EDS of the bare Ni mesh and the post-electrolysis Ni mesh cathode. (f) Atomic percentages (at.%) of different elements for the bare and post-electrolysis Ni mesh electrodes determined by SEM-EDS. Note: SEM-EDS shows a considerable increase in O content for the Ni cathode after electrolysis in the NaOH/KOH/H_2O electrolyte, but only a slight increase for the anode. The ~100 nm particles and 1–2.5 μm hexagonal flakes correspond to nickel oxides with different degrees of oxidation with Ni/O ratios of 3.66 and 0.72, respectively.
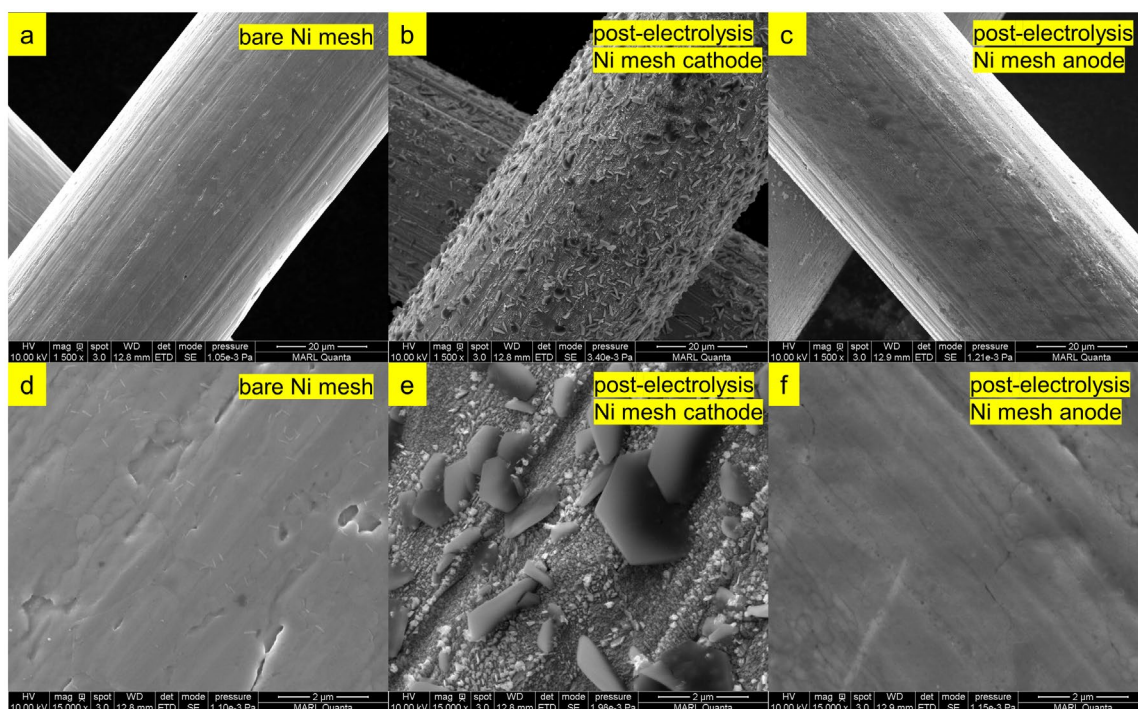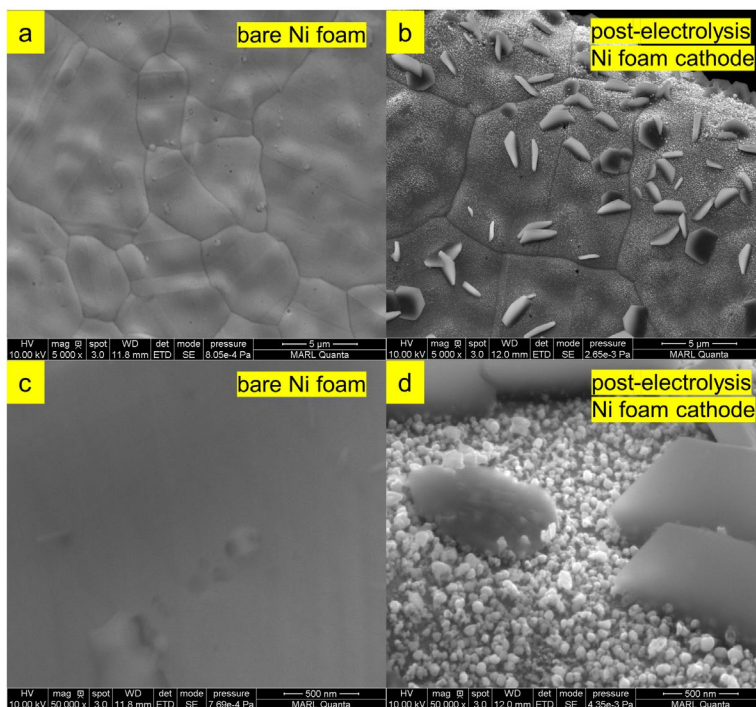
Fig. S15. SEM images of Ni foam electrodes. (a) Bare Ni foam before electrolysis. (b) Ni foam cathode after NO3RR measurement in the NaOH/KOH/H$_2$O electrolyte at 5 A cm^{-2}. (c)–(d) The corresponding images of (a)–(b) at higher magnification.

Sample	Ni (at.%)	O (at.%)	C (at.%)	Si (at.%)
post-electrolysis Ni foam cathode (sum)	62.86	24.08	12.35	0.71
post-electrolysis Ni foam cathode (area 1)	35.71	49.57	13.33	1.38
post-electrolysis Ni foam cathode (area 2)	80.06	7.41	12.03	0.50

Fig. S16. SEM-EDS analysis of the post-electrolysis Ni foam cathode. (a) SEM image of the post-electrolysis Ni foam cathode. (b)–(c) The corresponding elemental mappings of Ni and O. (d) EDS of the entire region (sum) and two selected areas of (a). (e) Atomic percentages (at.%) of different elements for the post-electrolysis Ni foam cathode determined by SEM-EDS.
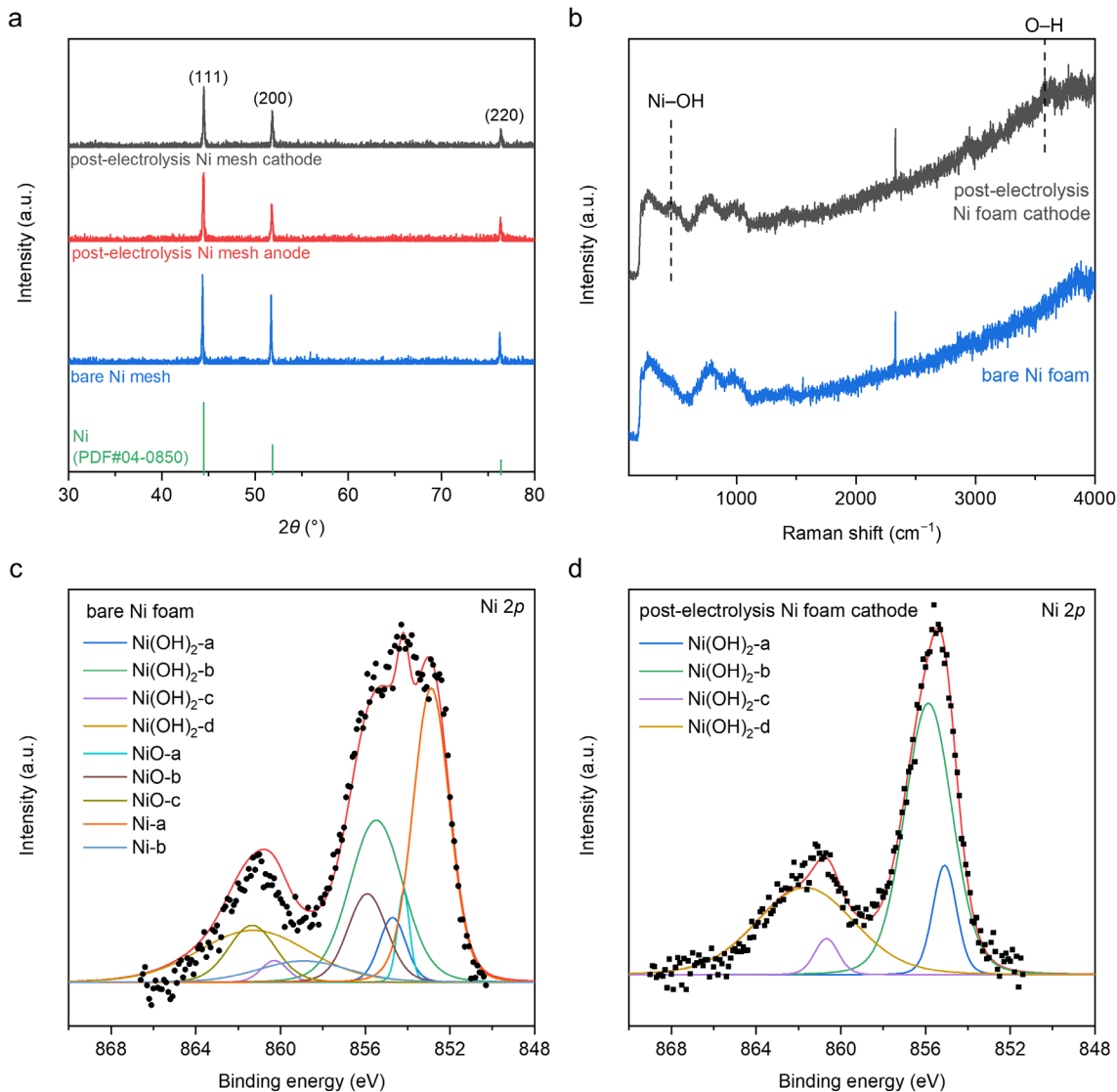
Fig. S17. Characterization of Ni electrodes before and after electrolysis in the NaOH/KOH/H$_2$O electrolyte. (a) XRD patterns of the bare Ni mesh and post-electrolysis Ni mesh electrodes. (b) Raman spectra of the bare Ni foam and post-electrolysis Ni foam electrodes. (c)–(d) Ni 2p XPS spectra of (c) the bare Ni foam and (d) post-electrolysis Ni foam electrodes. Note: for the post-electrolysis cathode, no emerging XRD peaks of nickel oxides or hydroxides were observed. Raman spectra show weak but identifia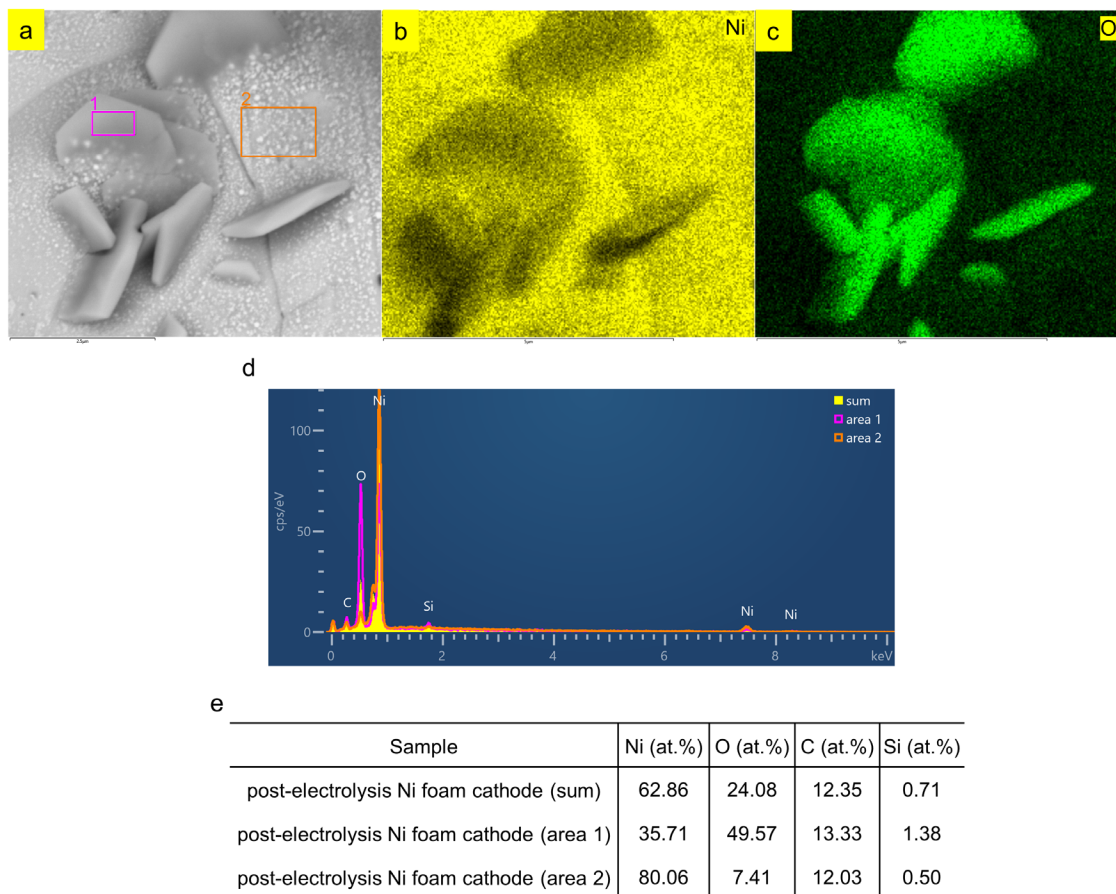ble signals at 450 and 3580 cm^{-1}, corresponding to the stretching modes of Ni–OH and O–H bonds, respectively.[15] XPS spectra show the apparent transformation from a mixture of metallic Ni and its oxides/hydroxides for the bare Ni foam surface, to a hydroxide-only surface for the post-electrolysis Ni foam cathode. These observations strongly suggest the formation of a Ni(OH)$_2$ layer on the Ni cathode surface after electrolysis in the NaOH/KOH/H$_2$O electrolyte.
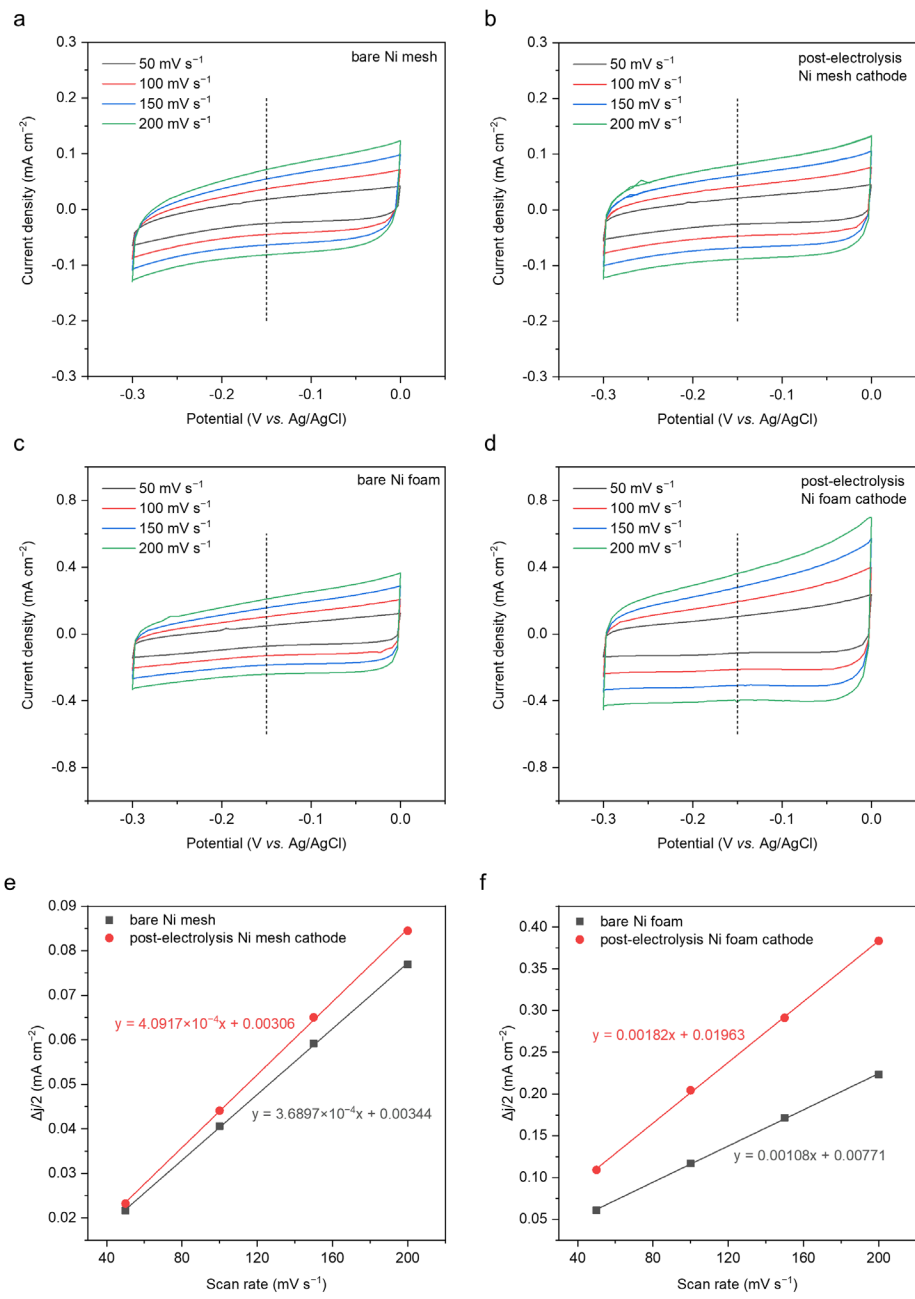
Fig. S18. Measurement of roughness factor (RF) of (a)–(b) Ni mesh and (c)–(d) Ni foam cathodes before and after electrolysis in the NaOH/KOH/H$_2$O electrolyte by cyclic voltammetry in 1 M KOH. (e)–(f) The corresponding capacitive currents at different scan rates for (e) Ni mesh and (f) Ni foam cathodes. The capacitive currents at −0.15 V *vs.* Ag/AgCl were used for RF calculation. Note: from the slope of (e) and (f), it was found that after electrolysis in the NaOH/KOH/H$_2$O electrolyte, the RF increases by 1.11 and 1.69 times for the Ni mesh and Ni foam cathode, respectively.

29
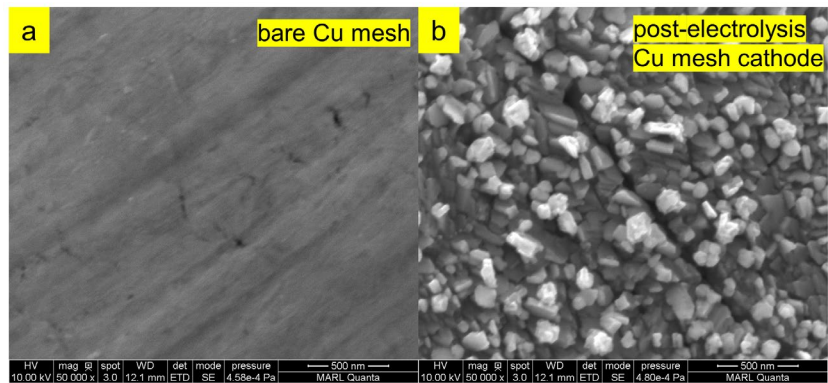
Fig. S19. SEM images of Cu mesh electrodes. The anode was a Ni mesh electrode. (a) Bare Cu mesh before electrolysis. (b) Cu mesh cathode after NO3RR measurement in the NaOH/KOH/H$_2$O electrolyte at 5 A cm^{-2}.
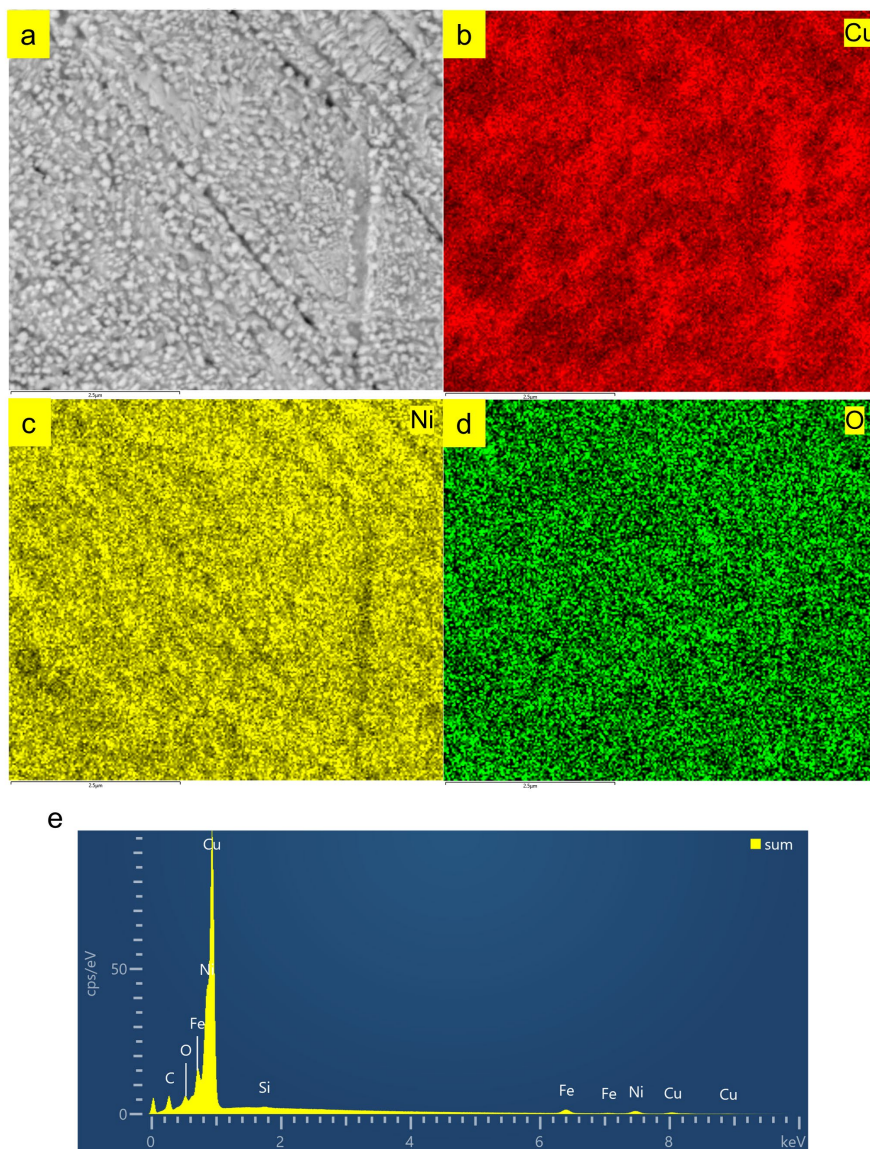
Fig. S20. SEM-EDS analysis of the post-electrolysis Cu mesh cathode. The anode was a Ni mesh electrode. (a) SEM image of the post-electrolysis Cu mesh cathode. (b)–(d) The corresponding elemental mappings of Cu, Ni, and O. (e) EDS of the entire region (sum) of (a). Note: SEM imaging and EDS suggest the deposition of nanostructured NiO_x on the Cu mesh cathode after electrolysis in the $NaOH/KOH/H_2O$ electrolyte. The Ni content on the post-electrolysis Cu mesh surface was 18.4 at.% (determined by SEM-EDS). Therefore, formation of the cathodic nanostructure should be attributed to the migration of Ni from anode to cathode during the electrolysis.
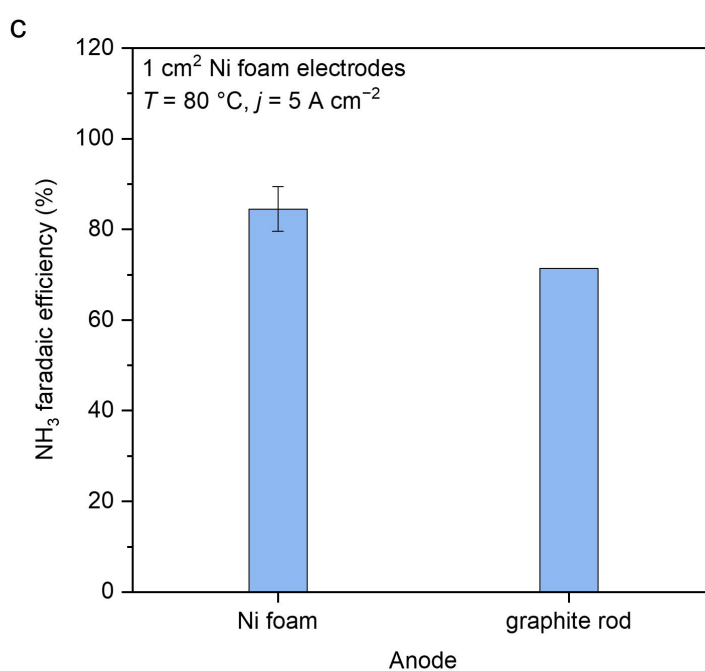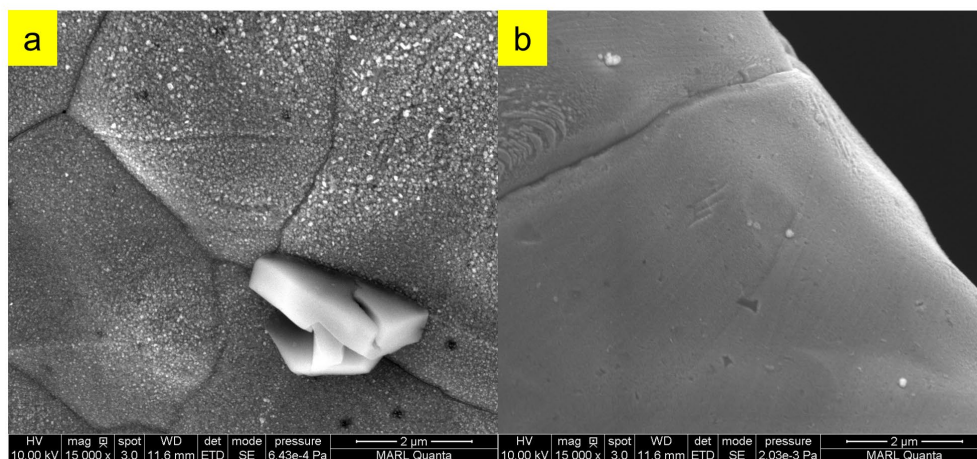
Fig. S21. Comparison of NO3RR on Ni foam cathode with different anodes. (a)–(b) SEM images of the post-electrolysis Ni foam cathode with (a) Ni foam and (b) graphite rod as the anode. (c) NH$_3$ FE at 5 A cm^{-2} on Ni foam cathode with different anodes. The diameter of the graphite rod was 1/4'', and its active area in the electrolyte was ~8.9 cm^2.
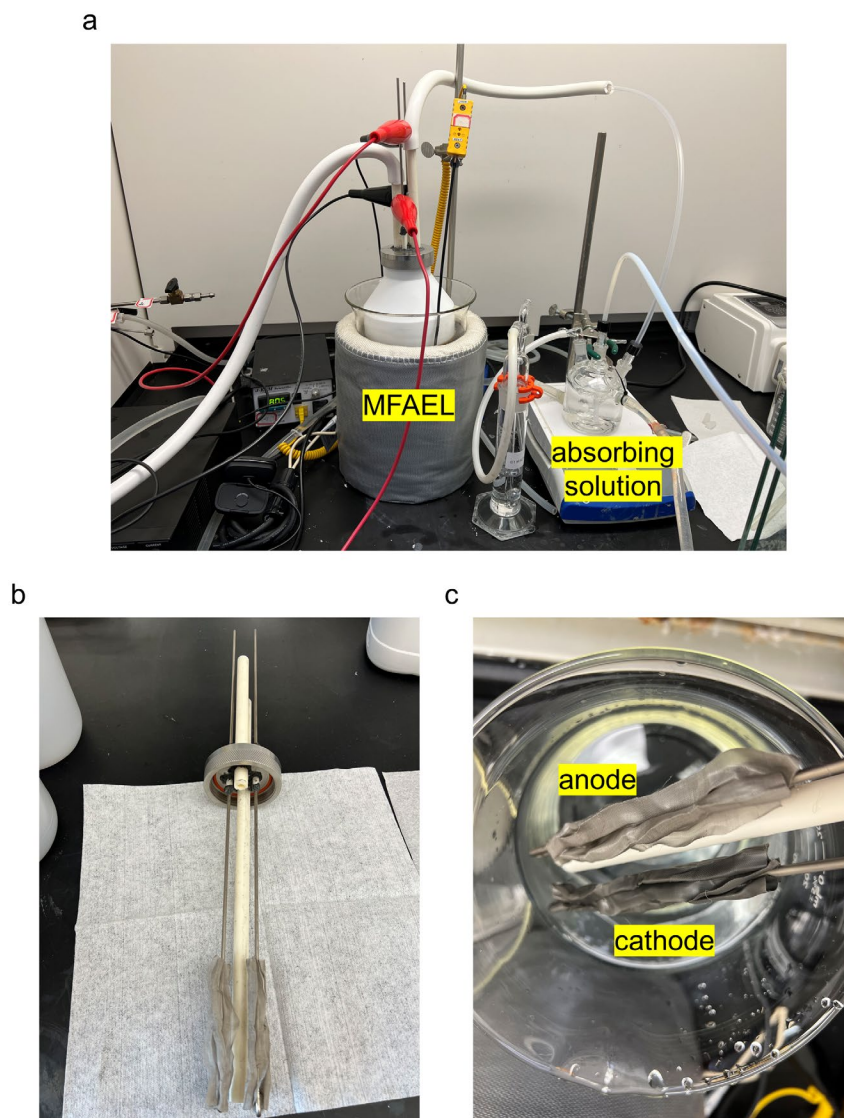
Fig. S22. Electrochemical NH_3 production by NO3RR in the scaled-up MFAEL system. (a) Photo of the scaled-up MFAEL system with a reactor capacity of 2.5 L. (b) Photo of the cell cap for the scaled-up MFAEL reactor. (c) Photo of the post-electrolysis Ni mesh electrodes. The darker color of the cathode suggests the formation of nanostructured NiO_x as a similar observation to the 100 mL reactor (Fig. S13).
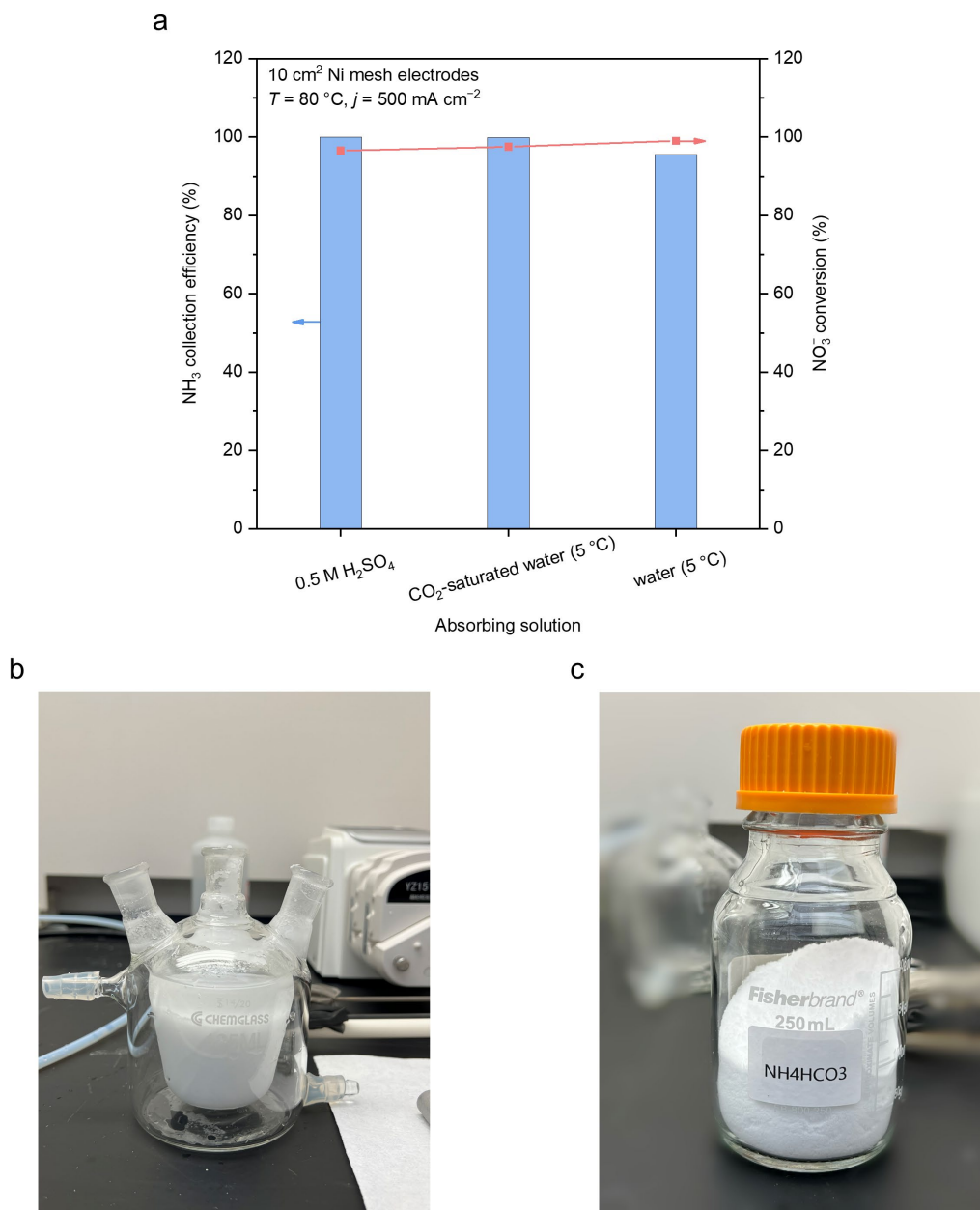
Fig. S23. Obtaining pure NH_3-based chemicals by using different absorbing solutions for the MFAEL system. (a) NH_3 collection efficiency for different absorbing solutions (100 mL for each): 0.5 M H_2SO_4, CO_2-saturated water (5 °C), and water (5 °C). The collection efficiency was determined by bubbling the outlet gas of the absorbing solution into an acidic solution (0.1 M H_2SO_4), and determining the ratio of NH_3 content between the absorbing solution and the acidic solution. Note that the NH_3 concentration in CO_2-saturated solutions was quantified by ^{1}H NMR due to the pH-sensitive nature of the colorimetric method. (b)–(c) Photos of the NH_4HCO_3 precipitate and obtained powder product by feeding the outlet gas from the scaled-up MFAEL into CO_2-saturated water at 5 °C.
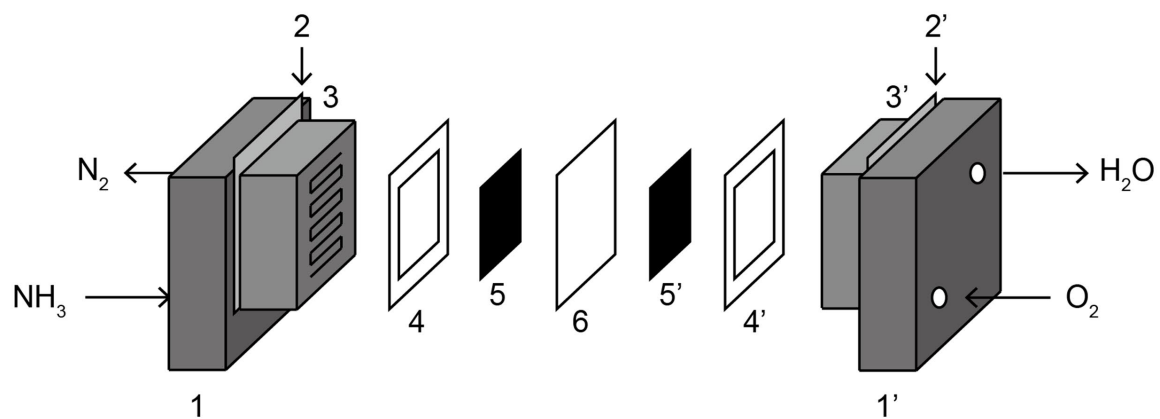
Fig. S24. The NH$_3$ fuel cell configuration, including end plates (1, 1'), current collectors (2, 2'), flow-field plates (3, 3'), gaskets (4, 4'), anode gas diffusion layer (5, PtIr/C on hydrophilic carbon cloth), cathode gas diffusion layer (5', Pt/C on carbon paper), and anion-exchange membrane (6, Tokuyama A201).
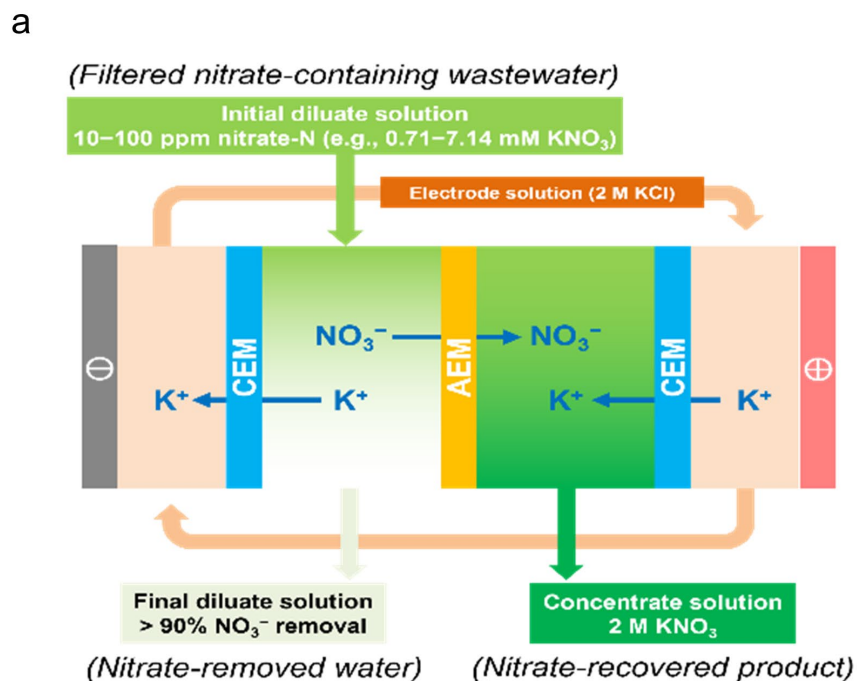
Fig. S25. Working principles of NO_3^- concentrating and the experimental electrodialysis system. (a) Schematic illustrating the working principles of NO_3^- concentrating via electrodialysis with one electrodialysis pair (CEM | diluate solution | AEM | concentrate solution), and one additional CEM (part of background cell). (b) Photo of our experimental electrodialysis system in operation encompassing one electrodialysis cell, two peristaltic pumps, and three solution containers (diluate, concentrate, and electrode solutions).
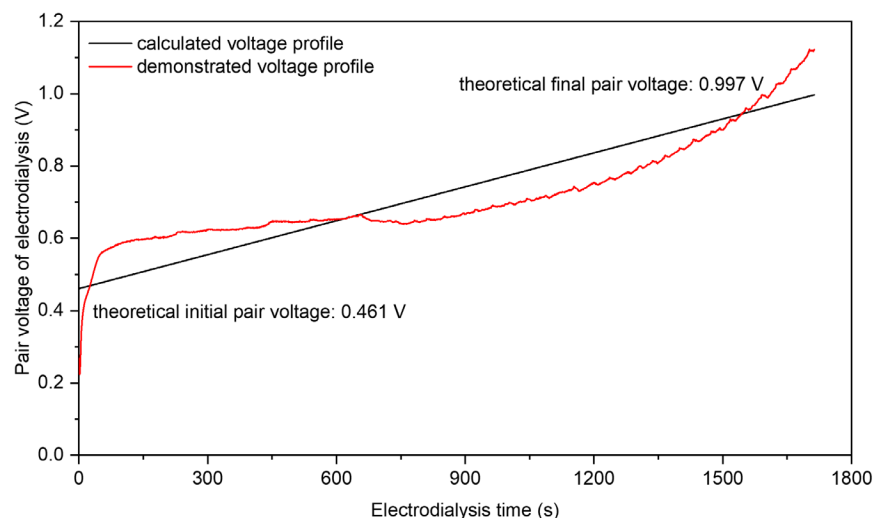
Fig. S26. The voltage profiles of one electrodialysis pair along with electrodialysis time for NO_3^- concentrating at 2 mA cm^{-2}. Note: a single electrodialysis pair is constructed by the configuration of "CEM | diluate | AEM | concentrate" in which the CEM and the AEM are FKA-PK-130 and FAA-PK-130, respectively, both from Fuma-Tech; and the diluate and the concentrate are 7.14 mM KNO_3 (containing 100 ppm NO_3^--N) and 2 M KNO_3 (28,000 ppm NO_3^--N), respectively. The key experimental conditions include: 5 cm^2 as the effective pair area (defined as the single surface of one membrane in the electrodialysis pair), 2 mA cm^{-2} as the electrodialysis current density, 10 cm s^{-1} as the nominal fluid velocity for all channels (60 mL min^{-1}), 0.5 mm as the distance between CEM and AEM in the electrodialysis pair, and 75% as the designed NO_3^- removal (1,722 s).

Fig. S27. Hierarchical structure of the TEA for NO_3^- concentrating by electrodialysis.

Name	Symbol	Value	Unit	Note	Source
OPEX-electrodialysis	OPEX-ed	1.46	$/kmol-NO3-		
OPEX-pumping	OPEX-p	0.56	$/kmol-NO3-		
OPEX-others	OPEX-o	0.20	$/kmol-NO3-	Assuming 10% of the sum of OPEX-pumping and OPEX-electrodialysis	
Operational Expense (OPEX)	OPEX	2.23	$/kmol-NO3-	OPEX = OPEX-p + OPEX-e + OPEX-o	
Levelized Capital Cost (LCC)	LCC	3.52	$/kmol-NO3-	Containing maintenance expense (a form of OPEX)	
Levelized Total Cost (LTC)	LTC	5.75	$/kmol-NO3-	LTC=LCC+OPEX	

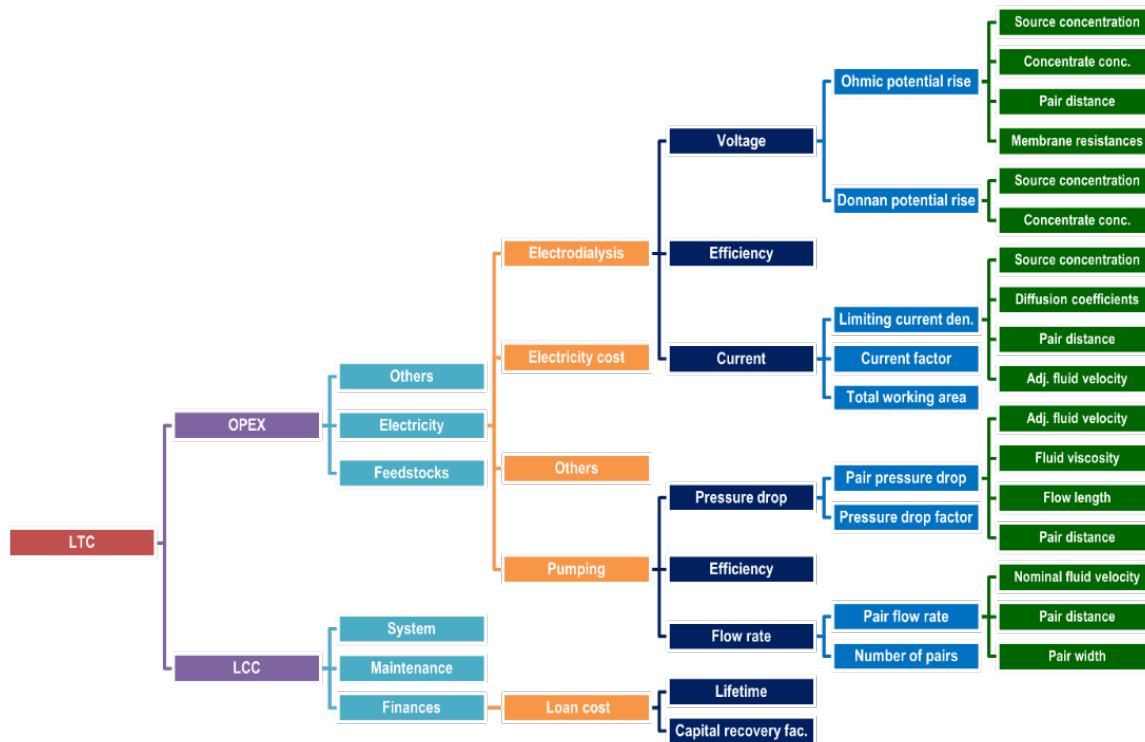| Name	Symbol	Value	Unit	Note	Source
Number of pairs	n	250			
Effective membrane-pair area	A-pair	4480	cm2/pair		
Total effective membrane-pair area	A-stack	112	m2/stack		
Membrane width	W	134	cm		
Membrane height/depth	H	33.5	cm		
Membrane distance	d	0.05	cm		
Nominal average velocity	V*	4	cm/s	Subjected to total cost minimization	
Area spacer porosity	ε-a	60	%		
Adjusted average velocity	V*'	6.7	cm/s		
AEM area resistance	R-AEM	2.5	Ωcm2		
CEM area resistance	R-CEM	2.5	Ωcm2		
Initial source concentration in ppm	Cs	100	ppm NO3-N	ppm NO3--N = mg NO3--N/L	
Initial source concentration in mM	Cs	7.14	mM	100 ppm-NO3--N/L = 7.14 mM	
Recovery efficiency	RE	80	%		
Final dilute concentration	Cd	1.43	mM		
Average source concentration	Cs*	4.29	mM		
Average source conductivity	σ-Cs°	0.48	mS/cm	σ = σ0*C*(-0.0315*lgC^2-0.2336lgC+0.5529), σ0 = 121.55 mS/cm	CRC Handbook
Nominal average diluate resistance	R-Cs°	103.3	Ωcm2		
Volume spacer porosity	ε-v	90	%		
Adjusted average diluate resistance	R-Cs°'	114.7	Ωcm2	σ = σ0*C*(-0.0315*lgC^2-0.2336lgC+0.5529), σ0 = 121.55 mS/cm	CRC Handbook
Average concentrate concentration	Cc°	2000	mM	Choosing 2 M as target concentration in concentrate	
Average concentrate conductivity	σ-Cc°	116.6	mS/cm		
Nominal average concentrate resistance	R-Cc°	0.43	Ωcm2		
Adjusted average concentrate resistance	R-Cc°'	0.48	Ωcm2		
Area resistance per effective pair	R-pair	120.2	Ωcm2	R-pair = R-AEM + R-CEM + R-Cs°' + R-Cc°'	
Resistance factor	fR	1.1		Assuming 10% additional resistance	
Overall area resistance per effective pair	R-pair'	132.2	Ωcm2	R-pair' = R-pair*fR	
Diffusion coefficient of NO3-	D-NO3	0.0000177	cm2/s	D = D°*(-0.0315*lgC^2-0.2336lgC+0.5529), D°= 1.90 x 10^-5 cm2/s	CRC Handbook
Average limiting current density	iL°	2.071	mA/cm2	iL° = 4.66*F*Cs°*(D°2/3)*(V°'d*H)^1/3	Rosenberg and Tirrell method (1957)
Average current density	i	1.86	mA/cm2	i = iL°*0.9	Environ. Sci. Water Res. Tech., 2019, 5, 1172
Total average stack-current	Is	8.35	A		
Donnan potential across membrane pair	φDon	0.315	V	φDon = 2*0.059*lg(Cc°/Cs°)	
Nominal electrodialysis voltage per pair	E-pair	0.561	V	E-pair = iL*R-pair' + φDon	Membranes, 2021, 11, 217.
Nominal electrodialysis voltage per stack	E-stack	140.4	V	E-pair = i*R-pair'*n	
Voltage efficiency	VE	80	%	Assuming 80% of voltage efficiency	
Adjusted electrodialysis voltage per stack	E-stack'	175.4	V	E-stack' = E-stack/VE	
Average electrodialysis power input per stack	P-stack	1464.9	W		
Daily operation time	t	24	h		
Coulombic efficiency	CE	90	%		
Daily production rate of NO3- in mole	r-mol-d	1.682	kmol-NO3-/day		
Daily production rate of NO3- in mass	r-mass-d	104	kg-NO3-/day	2-5 M depending on requirement	
Daily electrodialysis energy	Ee	35.157	kWh/day		
Energy intensity from electrodialysis		20.90	kWh/kmol-NO3-		
Electricity cost		0.070	$/kWh		
Electrodialysis energy cost	OPEX-ed	1.46	$/kmol-NO3-		

Name	Symbol	Value	Unit	Note	Source
Number of pairs	n	250			
Effective membrane-pair area	A-pair	4480	cm2/pair		
Total effective membrane-pair area	A-stack	112	m2/stack		
Membrane width	W	134	cm		
Membrane height/depth	H	33.5	cm		
Membrane distance	d	0.05	cm		
Nominal average velocity	V*	4	cm/s		Membranes, 2021, 11, 217.
Area spacer porosity	ε-a	60	%		
Adjusted average velocity	V*'	6.7	cm/s		
Adjusted channel diameter	dch	0.023	cm	dch = 4*ε/((2/d)+(1-ε)*(8/d))	Energy Procedia, 2012, 20, 170.
Re	Re	33.3		Re = ρ*V*'*d/μ, Re <= 1,400, ρ = 1,000 kg/m3	
Flow rate per pair	q	1.608	L/min		
Flow rate per stack	Q	670	L/min		
Pressure drop per pair	Δp-ch	20130	Pa	delta-P = 48*μ*V*'*H/(dch^2), μ = 0.001 Pa.s	J Membrane Sci, 2014, 462, 96.
Pressure drop factor	fp	0.5		fp = 0.5	J Membrane Sci, 2014, 462, 96.
Total pressure drop	Δp	40260	Pa	Δp = Δp-ch/fp	
Hydraulic power	Ph	449.57	W	Ph = Δp*Q	
Pumping efficiency	ηp	0.8	W	Assuming 80% of pumping efficiency	
Pumping power	Pp	561.96	W	Pp = Ph/ηp	
Initial source concentration	Cs	7.14	mM	100 ppm-NO3--N/L = 7.14 mM	
Recovery efficiency	RE	80	%	Assuming 80% of recovery efficiency	
Final dilute concentration	Cd	1.43	mM		
Average source concentration	Cs*	4.29	mM		
Source volume per 1 kmol-NO3- recovery	Vs*	175.0	m3	per 1 kmol-NO3- recovery	
Average current density	i	1.86	mA/cm2		
Total average stack-current	Is	8.35	A		
Daily operation time	t	24	h		
Coulombic efficiency	CE	90	%		
Daily production rate of NO3- in mole	r-mol-d	1.682	kmol-NO3-/day		
Daily production rate of NO3- in mass	r-mass-d	104.3	kg-NO3-/day	2-5 M depending on requirement	
Total volume of source feed	Vs-d	294.4	m3/day		
Daily pumping energy consumption	Ep	13.487	kWh		
Pumping energy intensity		8.02	kWh/kmol-NO3-		
Electricity cost		0.070	$/kWh		
Pumping energy cost	OPEX-p	0.56	$/kmol-NO3-		

Name	Symbol	Value	Unit	Note	Source
Cost of commercial electrodialysis system	Ccap-ED	35,000	$/system	Hangzhou Iontech Environmental Technology Co., Ltd.	Alibaba.com
Number of pairs	n	250	pair		
Dimension of membrane - width	W	40	cm		
Dimension of membrane - height	H	160	cm		
Gross membrane-pair area	A'-pair	6400	cm2/pair		
Effective-to-gross area ratio	β	70	%		
Effective membrane-pair area	A-pair	4480	cm2/pair		
Total effective pair-area per stack	A-stack	112	m2/stack		
Average current density	i	1.86	mA/cm2		
Total average stack-current	Is	8.35	A		
Coulombic efficiency	CE	90	%		
Daily production rate of NO3-	r-mol-d	1.682	kmol-NO3-/day		
Capacity factor	CF	83.3	%	300 days a year	
Annual production rate of NO3-	r-mol-a	511	kmol-NO3-/year	rmol-a = rmol-d*365*CF	
Cost ratio of maintenance to system	γ	19	%	19%, based on the average of 27% and 11%	J. Environ. Qual., 2017, 46, 1528.
Cost of total maintenance	Cmain-ED	6650	$	replacement/repair of some membranes & parts	J. Environ. Qual., 2017, 46, 1528.
Total present value of cost (TPVC)	TPVC	41,650	$	TPVC = Ccap-ED + Cmain-ED	Water Resour. Econ., 2013, 2-3, 30.
Time of service	t	40	year		
Annual discount rate	α	3	%	3% for real and 2.5% for nominal	2013 publication: NISTIR - 85-3273-28
Capital recovery factor (CRF)	CRF	0.0433		CRF = m*(1 + α)^m/((1 + α)^m - 1)	
Equal annual cost (EAC)	ECA	1801.88	$	ECA = TPVC*CRF	Water Resour. Econ., 2013, 2-3, 30.
Levelized capital cost (LCC)	LCC	3.52	$/kmol-NO3-	LCC = ECA/rmol-a	

Fig. S28. TEA results for NO_3^- concentrating by electrodialysis. Summary (top) and detailed calculations and assumptions (bottom) for OPEX components and LCC.
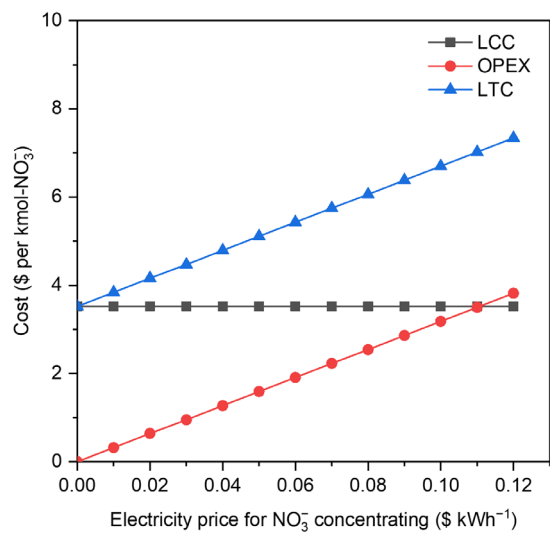
Fig. S29. The impact of electricity price on LTC and OPEX for NO_3^- concentrating by electrodialysis (assuming 100 ppm NO_3^--N of diluate, and 80% of designed NO_3^- recovery).
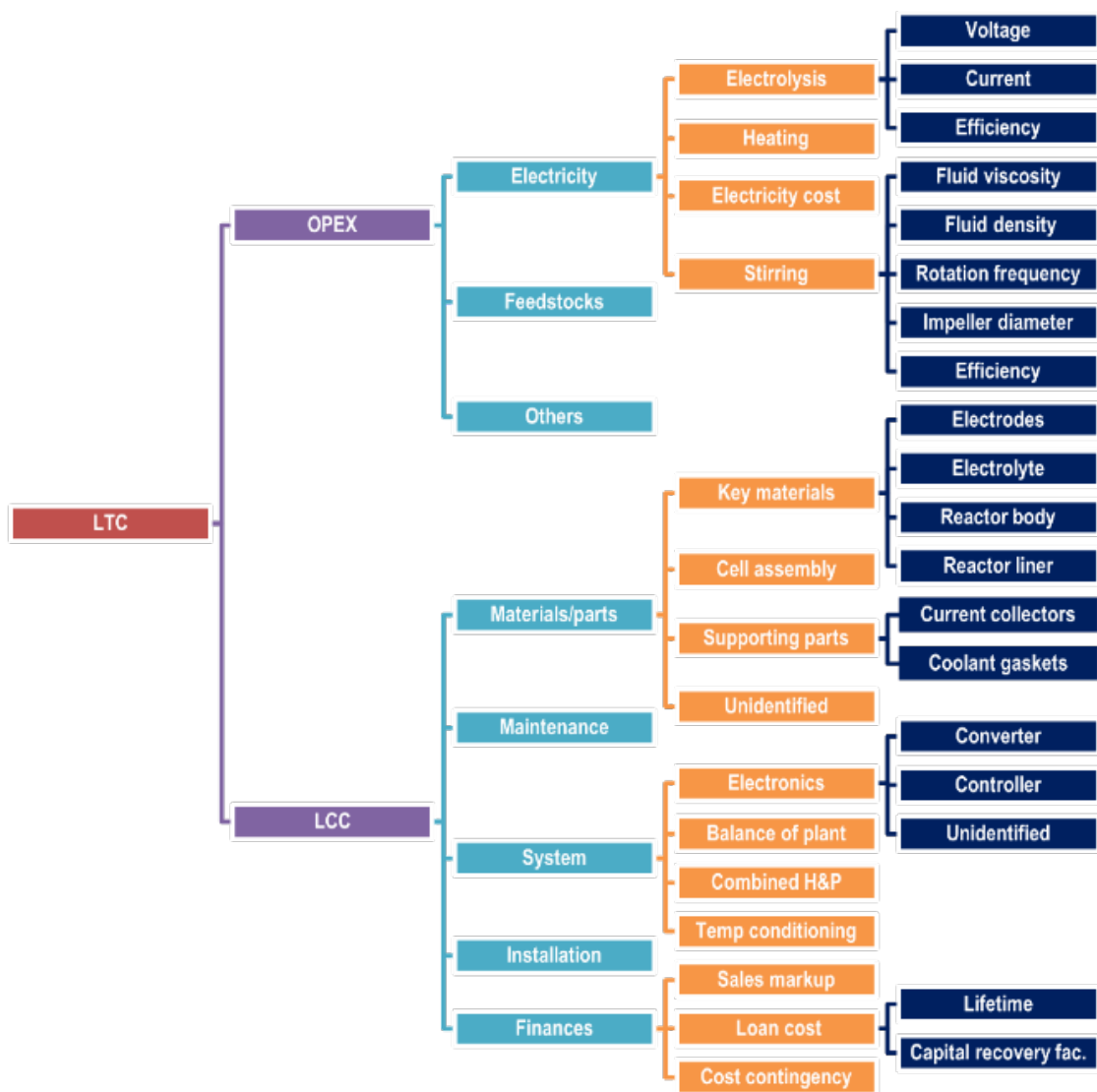
Fig. S30. Hierarchical structure of the TEA for NO_3^--to-NH_3 conversion by electrolysis in MFAEL.

Name	Symbol	Value	Unit	Note	Source
OPEX-electrolysis	OPEX-el	45.03	$/kmol-NH3		
OPEX-mixing	OPEX-m	0.17	$/kmol-NH3		
OPEX-heating	OPEX-h	2.25	$/kmol-NH3		
Operational Expenses (OPEX)	OPEX	47.45	$/kmol-NH3	OPEX = OPEX-el + OPEX-m + OPEX-h	
Levelized Capital Cost (LCC)	LCC	0.97	$/kmol-NH3	Containing maintenance expense (a form of OPEX)	
Levelized Total Cost (LTC)	LTC	48.42	$/kmol-NH3	LTC = LCC + OPEX	

Name	Symbol	Value	Unit	Note	Source
Electrode area per fin	A-fin	2800	cm2/fin	40 cm x 35 cm x 2	
Number of electrode fins	n	12	fin/cell		
Total area of electrode	A-cell	33600	cm2/cell		
Current density	i	250	mA/cm2		
Total current	I-cell	8400	A/cell		
Number of cells per pack	m	1			
Operation temperature	T	120	oC		
Cell voltage	E	2.70	V		
Power of electrolysis	P-electrolysis	22.68	kW		
Daily operation time	t	24	h		
Coulombic efficiency	CE	90	%		
Daily production rate of HN3 in mole	r-mol-d	0.846	kmol-NH3/day		
Daily production rate of NH3 in mass	r-mass-d	14.4	kg-NH3/day		
Daily electrolysis energy	Ee	544.320	kWh/day		
Energy intensity from electrolysis		643.23	kWh/kmol-NH3		
Electricity cost		0.070	$/kWh		
OPEX-electrolysis	OPEX-el	45.03	$/kmol-NH3		
Density	ρ	1.51	g/cm3	ρ = 1.61061 - 0.0008*T	See *
Viscosity	μ	1.85	mPa.s	μ = 2341.3*(T^(-1.492))	See *
Diameter of impeller	di	15.00	cm		
Rotation frequency	rps	5.00	round/s		
Reynolds # (Re)	Re	92074		Re = di^2*rps*d/μ, Re < 10	
Froude # (Fr)	Fr	0.3823		Fr = ρ*rps^2/g, g = 9.81 m/s2	
Power #, P0	P0	6		P0 = 6, when Re > 6,000	Food Process Engineering and Technology, 2009
Power of stirring	P-stirring	0.086	kW	P = P0*di^5*rps^3*ρ	
Daily stirring energy	Es	2.07	kWh		
Energy intensity from stirring		2.45	kWh/kmol-NH3		
OPEX-mixing	OPEX-s	0.17	$/kmol-NH3		
Power of heating	P-heating	1.134	kW	5% of electrolysis power	
Daily stirring energy	Es	27.22	kWh		
Energy intensity from heating		32.16	kWh/kmol-NH3		
OPEX-heating	OPEX-h	2.25	$/kmol-NH3		
Operational Expenses (OPEX)	OPEX	47.45	$/kmol-NH3		

Proceedings of International conference: CFCs; F. COTANA, ASDRUBALI F., & SANTARPIA L (1994). Thermophysical properties of H2O-NaOH-KOH mixtures: experimental data.

Name	Symbol	Value	Unit	Note	Source
Power rating per cell	Pcell	22.77	kW		
Total area of electrode	A-cell	3.360	m2/cell		
Price of cathode material		29.97	$/m2	Nickel cloth with 200 mesh count, current price	www.made-in-china.com
Cost of cathode materials	C-cm	100.70	$/cell		
Price of anode material		29.97	$/m2	Nickel cloth with 200 mesh count, current price	www.made-in-china.com
Cost of anode materials	C-am	100.70	$/cell		
Volume of NaOH-KOH-H2O electrolyte	Ve	100	L	50 cm x 50 cm x 40 cm	
Density of NaOH-KOH-H2O electrolyte	ρ	1.51	g/cm3		
Weight of NaOH		37.87	kg/cell	25wt.% in NaOH, based on 40wt.% in H2O	
Price of NaOH		282	$/ton-NaOH	Five-year average 2016-2020	tradingeconomics.com
Cost of NaOH		10.68	$/cell		
Weight of KOH		53.01	kg/cell	35wt.% in NaOH, based on 40wt.% in H2O	
Price of KOH		235.6	$/ton-KOH	Five-year average 2016-2020	www.statista.com
Cost of KOH		12.49	$/cell		
Cost of NaOH-KOH-H2O electrolyte	C-electrolyte	23.17	$/cell		
Volume of PTFE		0.0125	m3/cell	50 cm x 50 cm x 40 cm @ 1 cm	
Weight of PTFE		27.5	kg/cell	Based on 2.2 g/cm3 of PTFE density	
Price of cell body - PTFE		13,000	$/ton	2017 price	www.statista.com
Cost of cell body - PTFE	C-body	357.50	$/cell		
Volume of stainless steel		0.0125	m3/cell	50 cm x 50 cm x 40 cm @ 1 cm	
Weight of stainless steel		97.5	kg/cell	Based on 7.8 g/cm3 of stainless steel density	
Price of cell body - stainless steel		536	$/ton	Five-year average 2015-2019	www.focus-economics.com
Cost of cell body - stainless steel	C-liner	52.22	$/cell		
Power of stirring	P	86	W		
Cost of stirring motor and parts	C-stirrer	47.50	$/cell	100-W motor, and corrosion-resistant rod/blades	picclick.com
Cost of coolant gaskets	C-gasket	37.00	$/cell		Strategic Analysis Report: $37/stack
Cost of cell assembly	C-assembly	33.00	$/cell		Strategic Analysis Report: $33/stack
Cost of temperature conditioning	C-conditioning	42.00	$/cell		Strategic Analysis Report: $42/stack
Cost of current collectors	C-collector	4.00	$/cell		Strategic Analysis Report: $4/stack
Cost of Balance-Of-Plant (BOP)	C-BOP	29.40	$/cell		Strategic Analysis Report: $29.40/stack
Cost of Combined Heat and Power (CHP)	C-CHP	10.61	$/cell		Strategic Analysis Report: $10.61/stack
Cost of Power Electronics (PE)	C-PE	325.90	$/cell		Strategic Analysis Report: $325.90/stack
Cost of all identified materials and parts	C-m&p	1163.70	$/cell		Strategic Analysis Report
Cost of all other parts and minor materials	C-others	116.37	$/cell	10% of all identified materials and parts	
Cost Contingency	C-CC	128.01	$/cell	10% of the cost of all materials and parts	Strategic Analysis Report
Sales Markup (SM)	C-SM	816.68	$/cell	50% of the cost of all materials and parts & sales markup	Strategic Analysis Report
Cost of System Installation	C-SI	896.05	$/cell	70% of the cost of all materials and parts	Strategic Analysis Report
Capital Expenses, CAPEX	CAPEX	3120.80	$/cell		
Average current density	i	250	mA/cm2		
Total average stack-current	Is	8400	A		
Coulombic efficiency	CE	90	%		
Daily production rate of NH3	r-mol-d	0.846	kmol-NH3/day		
Capacity factor	CF	83.33	%	300 days a year	
Annual production rate of NH3	r-mol-a	257	kmol-NH3/year	rmol-a = rmol-d*365*CF	
Cost ratio of maintenance to system	γ	19	%	Assuming 19% fo total capital cost	
Cost of total maintenance	Cmain-El	592.95	$	Replacement/repair of some electrodes & parts	J. Environ. Qual., 2017, 46, 1528.
Total present value of cost (TPVC)	TPVC	3,714	$	TPVC = Ccap-ED + Cmain-ED	Water Resour. Econ., 2013, 2-3, 30.
Time of service	t	20	year		
Annual discount rate	α	3	%	3% for real and 2.5% for nominal	2013 publication: NISTIR - 85-3273-28
Capital recovery factor (CRF)	CRF	0.0672		CRF = m*(1 + α)^m/((1 + α)^m - 1)	
Equal annual cost (EAC)	ECA	249.62	$	ECA = TPVC*CRF	Water Resour. Econ., 2013, 2-3, 30.
Levelized Capital Cost (LCC)	LCC	0.97	$/kmol-NH3	LCC = ECA/rmol-a	

Fig. S31. TEA results for NO_3^--to-NH_3 conversion by electrolysis in MFAEL. Summary (top) and detailed calculations and assumptions (bottom) for OPEX components and LCC.
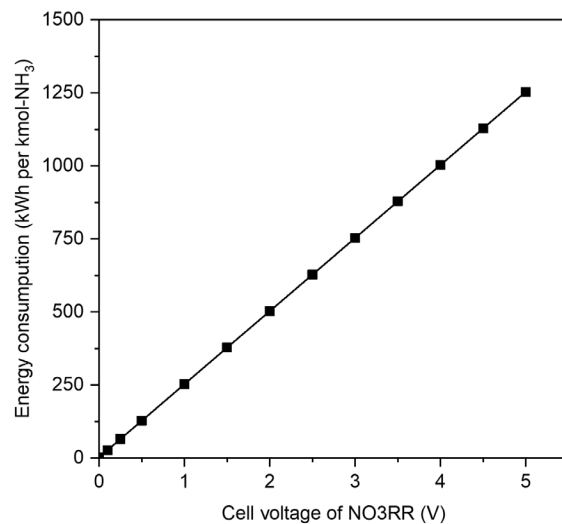
Fig. S32. The energy consumption of NO3RR as a function of the cell voltage (with 5% heating-to-electrolysis ratio).
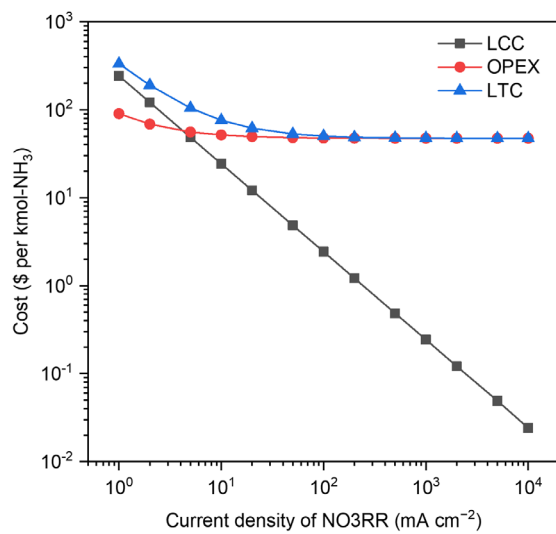
Fig. S33. LTC, OPEX, and LCC of NO3RR in $ per kmol-NH$_3$ along with the electrolytic current density (assuming 2.7 V of cell voltage and $0.07 kWh^{-1} of electricity price).
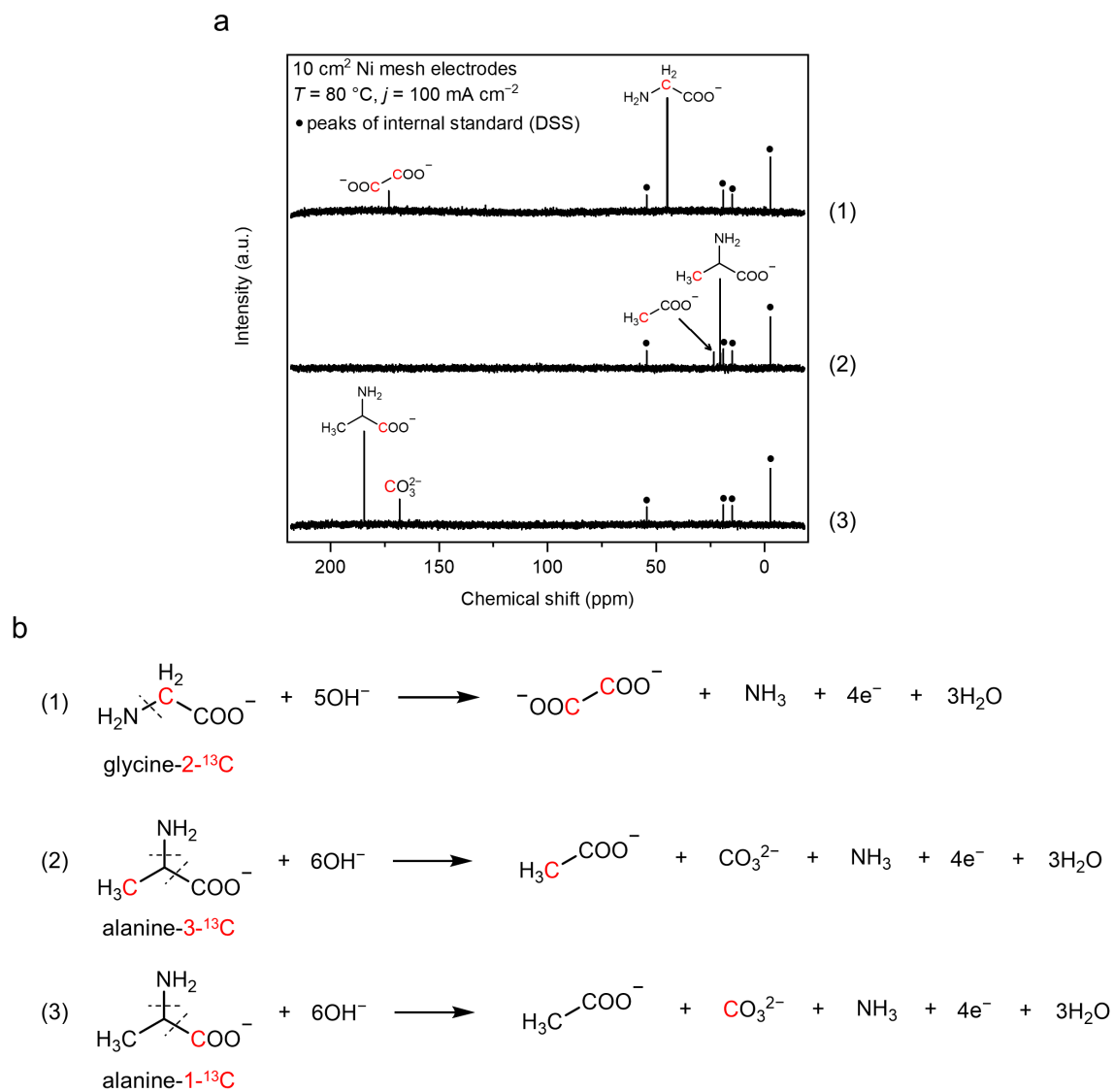
Fig. S34. Product investigation on the conversion of organic Nr compounds in the NaOH/KOH/H$_2$O electrolyte by ^{13}C NMR. Electrolysis was carried out with ^{13}C-labeled chemicals (4.2 mmol for glycine, or 6.7 mmol for alanine) for 1 h. (a) NMR spectra of the electrolyte after reaction with different ^{13}C-labeled reactants: (1) glycine-2-^{13}C, (2) alanine-3-^{13}C, and (3) alanine-1-^{13}C. (b) The identified half-reaction equations for (1)–(3). The isotopically labeled ^{13}C atoms are colored red, and the bond cleavages are represented by the dashed lines.
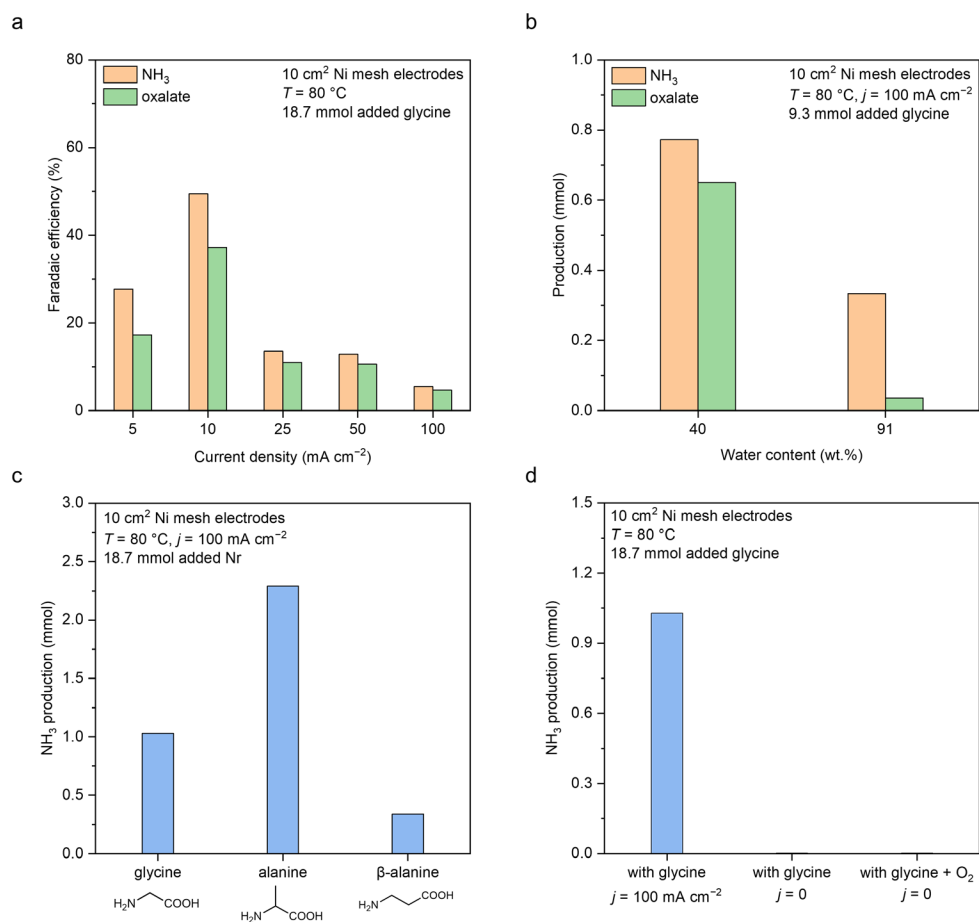
Fig. S35. Conversion of organic Nr compounds in the NaOH/KOH/H$_2$O electrolyte under different operating conditions. All tests were carried out for 2 h under the conditions specified in the figures. Oxalate production was determined by HPLC. (a) FE towards NH$_3$ and oxalate at different current densities with glycine as the reactant. (b) Effect of alkalinity (water content) on the production of NH$_3$ and oxalate from glycine. (c) NH$_3$ production from the conversion of glycine, alanine, and β-alanine. (d) Control experiments with 18.7 mmol of glycine as the reactant in the NaOH/KOH/H$_2$O electrolyte. From left to right: 1st column, with 100 mA cm^{-2} of applied current density. 2nd column, without applied current. 3rd column, with 200 mL min^{-1} of O$_2$ feed, and no applied current. Note: these results suggest that under the operating conditions of MFAEL, the ratio of NH$_3$ and oxalate production is close to 1, agreeing with the results from ^{13}C NMR (Fig. S34). High alkalinity and electricity are indispensable for the efficient conversion of C–N bonds, and such a process is not an O$_2$-mediated non-faradaic process. The secondary amine (alanine) shows a higher NH$_3$ production rate than the primary amine (glycine), and amine groups at α-C (such as amino acids) are much more reactive compared to those with longer carbon chains (such as β-alanine). These trends agree with the screening test results at 200 °C (Fig. 6b and Table S3).
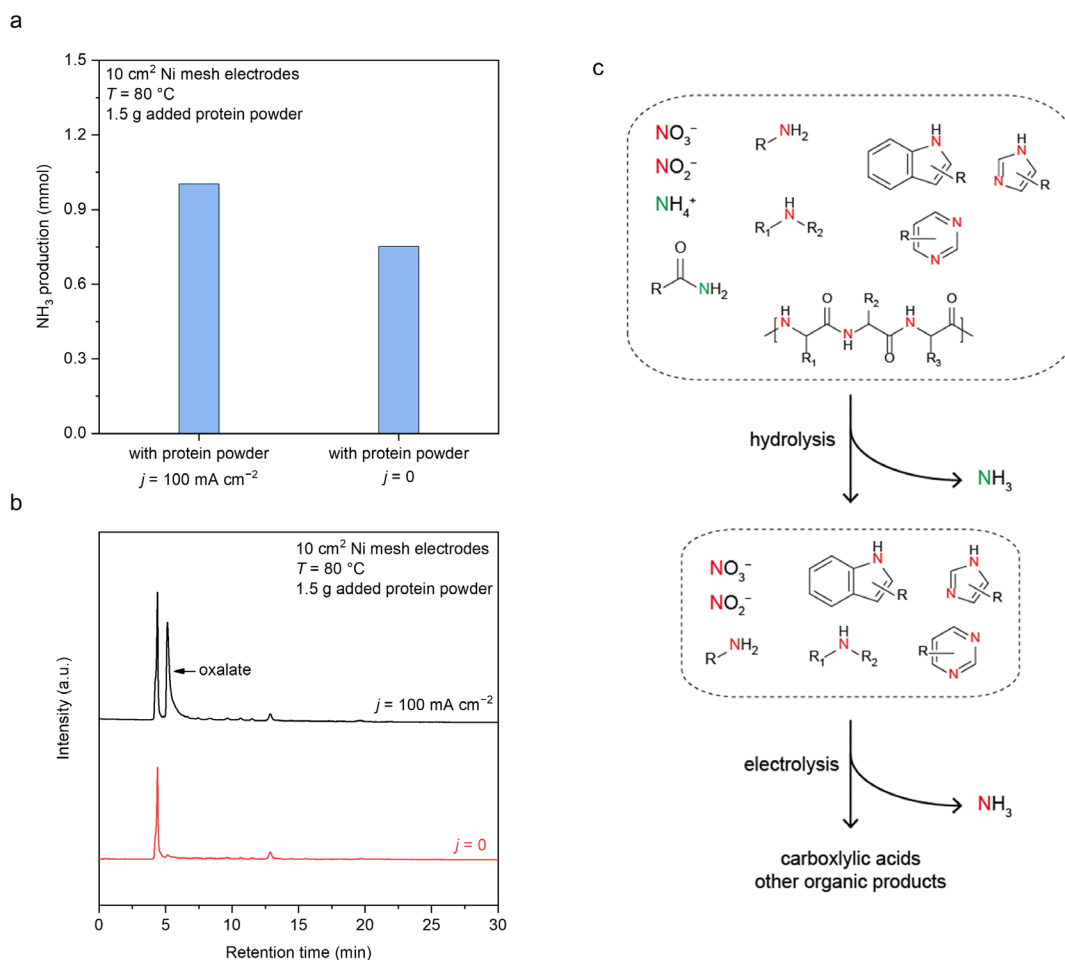
Fig. S36. Electrolysis in the NaOH/KOH/H$_2$O electrolyte with a commercial protein powder (Orgain). The content of N is 8.90 wt.% (determined by a combustion elemental analyzer). The reaction time was 2 h. (a) NH$_3$ production with and without 100 mA cm^{-2} of applied current density. (b) HPLC graphs of the electrolyte after reaction with and without 100 mA cm^{-2} of applied current density. (c) The suggested pathway for the conversion of different forms of Nr to NH$_3$ in the NaOH/KOH/H$_2$O electrolyte. Note: the protein powder sample contains various forms of Nr. As it was added into the electrolyte in MFAEL, NH$_3$ evolved instantly without applying current. As shown in the first step in (c), production of this NH$_3$ (colored green) should be contributed to the hydrolysis reaction of low-valent N (NH$_4^+$ ions and primary amide groups) in the sample, which occurs readily under the MFAEL operating conditions (high alkalinity and elevated temperature). Comparing the NH$_3$ production with and without applied current, it was found that electricity boosted the total NH$_3$ production by 33%, which is due to the oxidation of Nr in amino acids. Meanwhile, the carboxylic acid product (oxalate as identified in HPLC) is produced only with an applied current, verifying that the oxidation-assisted NH$_3$ production (by the cleavage of C–N bonds) requires the participation of electricity [colored red in (c)].
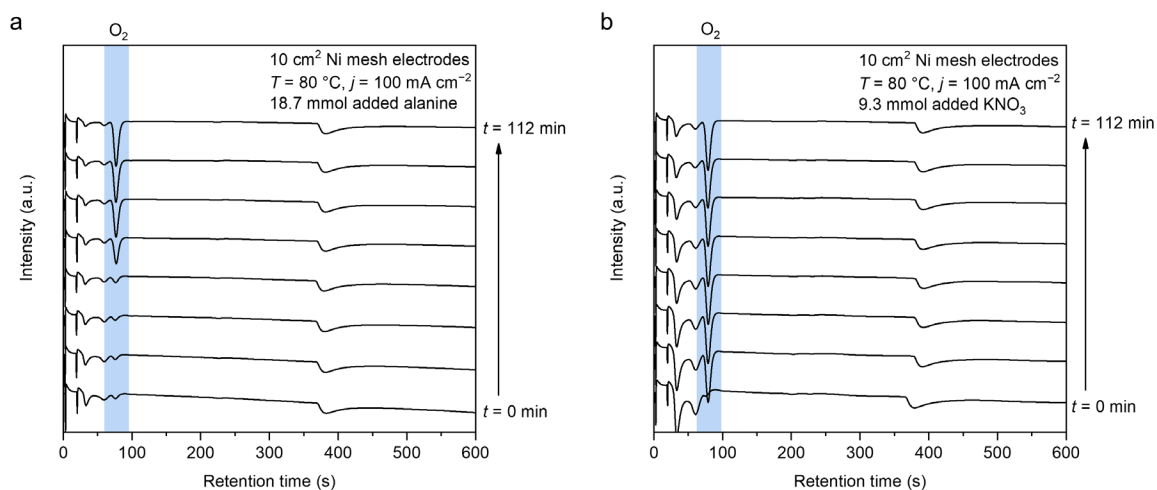
Fig. S37. Detection of O_2 for the conversion of organic Nr in the NaOH/KOH/H$_2$O electrolyte by online GC. Helium gas was used as the carrier gas for both MFAEL and GC. GC graphs with thermal conductivity detector (TCD) during the electrolysis with (a) alanine and (b) KNO$_3$. Production of O_2 from OER is apparently suppressed in the presence of organic Nr (alanine), while it remains stable in the absence of organic Nr.
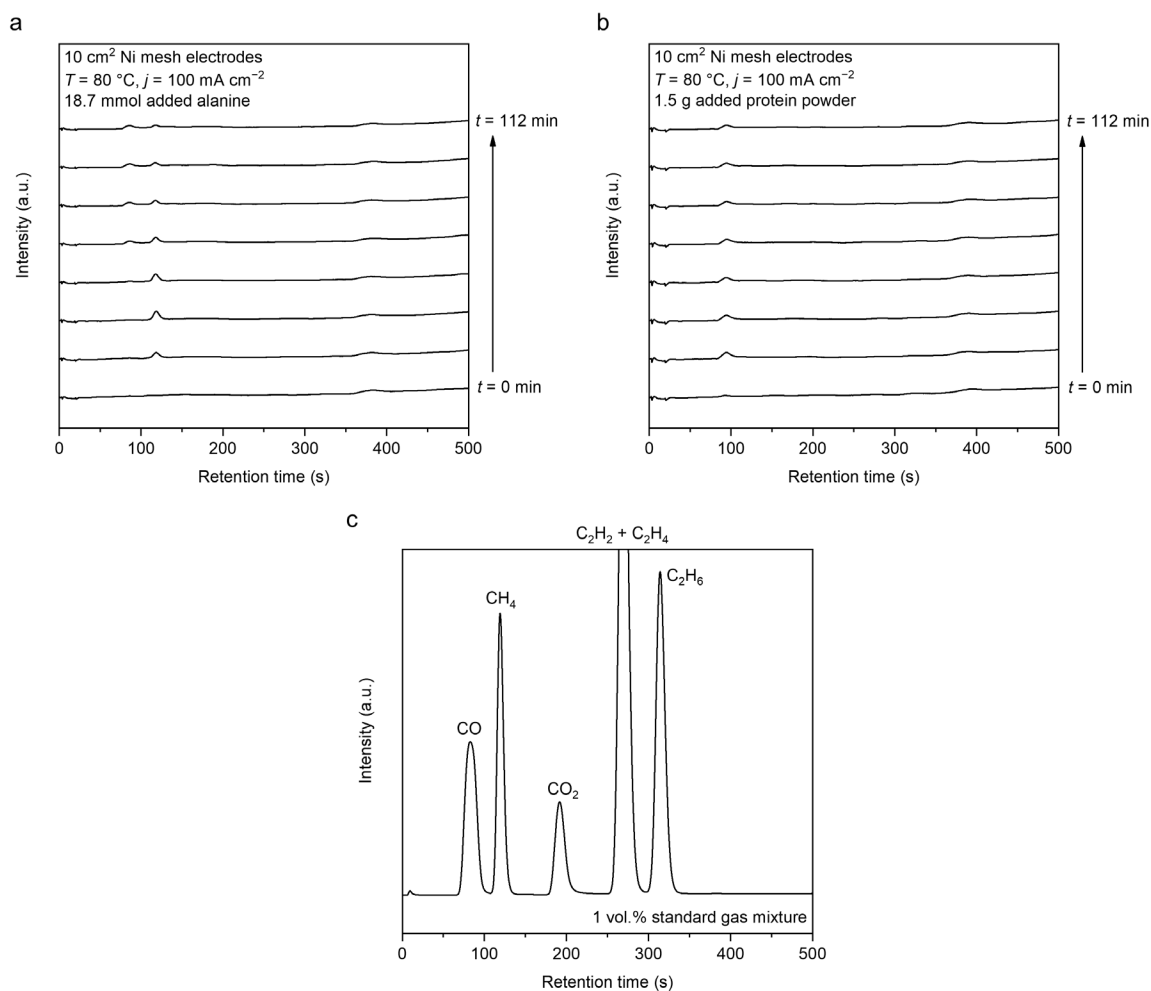
Fig. S38. Detection of volatile carbon-containing products for the conversion of organic Nr in the NaOH/KOH/H$_2$O electrolyte by online GC. Helium gas was used as the carrier gas for both MFAEL and GC. GC graphs with flame ionization detector (FID) during the electrolysis with (a) alanine and (b) protein powder. (c) GC graph of the standard 1% gas mixture of CO, CH$_4$, CO$_2$, C$_2$H$_2$, C$_2$H$_4$, and C$_2$H$_6$ (in N$_2$ balance), with the same zoom scale as (a) and (b). Despite its ppm-level sensitivity, no known volatile carbon-containing product was detected by FID during the conversion of organic Nr, indicating that carbon is retained in the electrolyte.
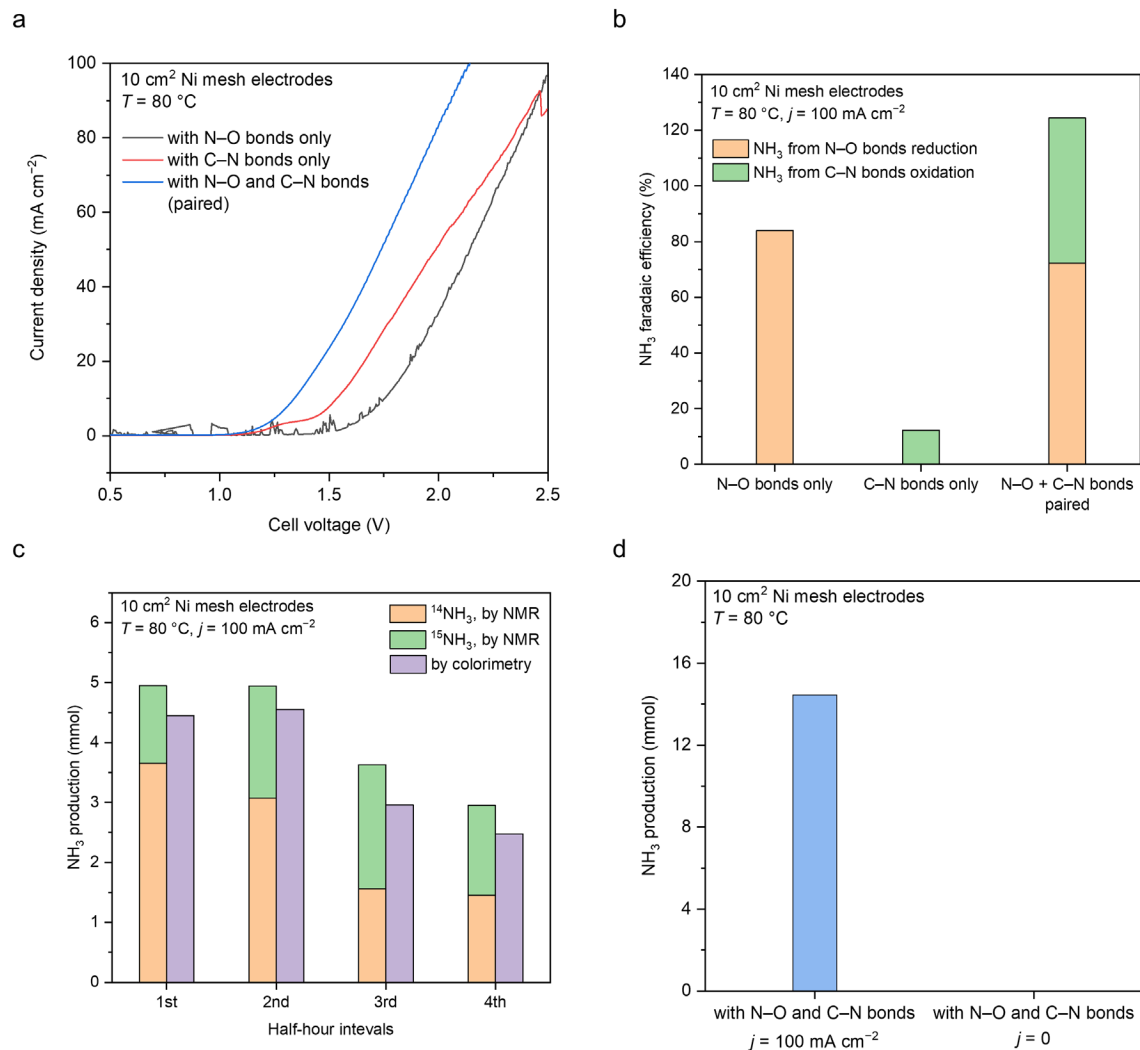
Fig. S39. Electrolysis with different Nr compounds containing N–O or C–N bonds. KNO₃ (9.3 mmol) and alanine (18.7 mmol) were chosen as the model chemicals containing N–O and C–N bonds, respectively. The reaction time was 2 h. (a) LSV curves for the NaOH/KOH/H₂O electrolyte containing different forms of Nr. (b) The FE towards NH₃ (single-electrode basis) for the electrolysis with different added Nr compounds. From left to right: 1st column, containing N–O bonds only; 2nd column, containing C–N bonds only; 3rd column, containing both N–O and C–N bonds. (c) Comparison of NH₃ production determined between ¹H NMR and colorimetry at different stages of electrolysis for the system containing ¹⁵N–O and C–¹⁴N bonds. (d) NH₃ production with and without 100 mA cm⁻² of applied current density. Note: ¹H NMR suggested that NH₃ comes from the cleavage of both N–O and C–N bonds. Comparison of different quantification methods shows the accuracy of both ¹H NMR and colorimetry methods. Compared to the system with only one added component, the FE of NO3RR slightly decreases (84.0% *vs.* 72.3%), while the FE of alanine oxidation increases considerably (12.3% *vs.* 52.1%). Such a synergetic effect for the paired system is possibly due to the difference in electrode potentials. The synergy could also come from the suppression of certain side reactions (such as HER or OER) that affect the reaction pathway towards NH₃ by stabilizing or destabilizing the reaction intermediates.
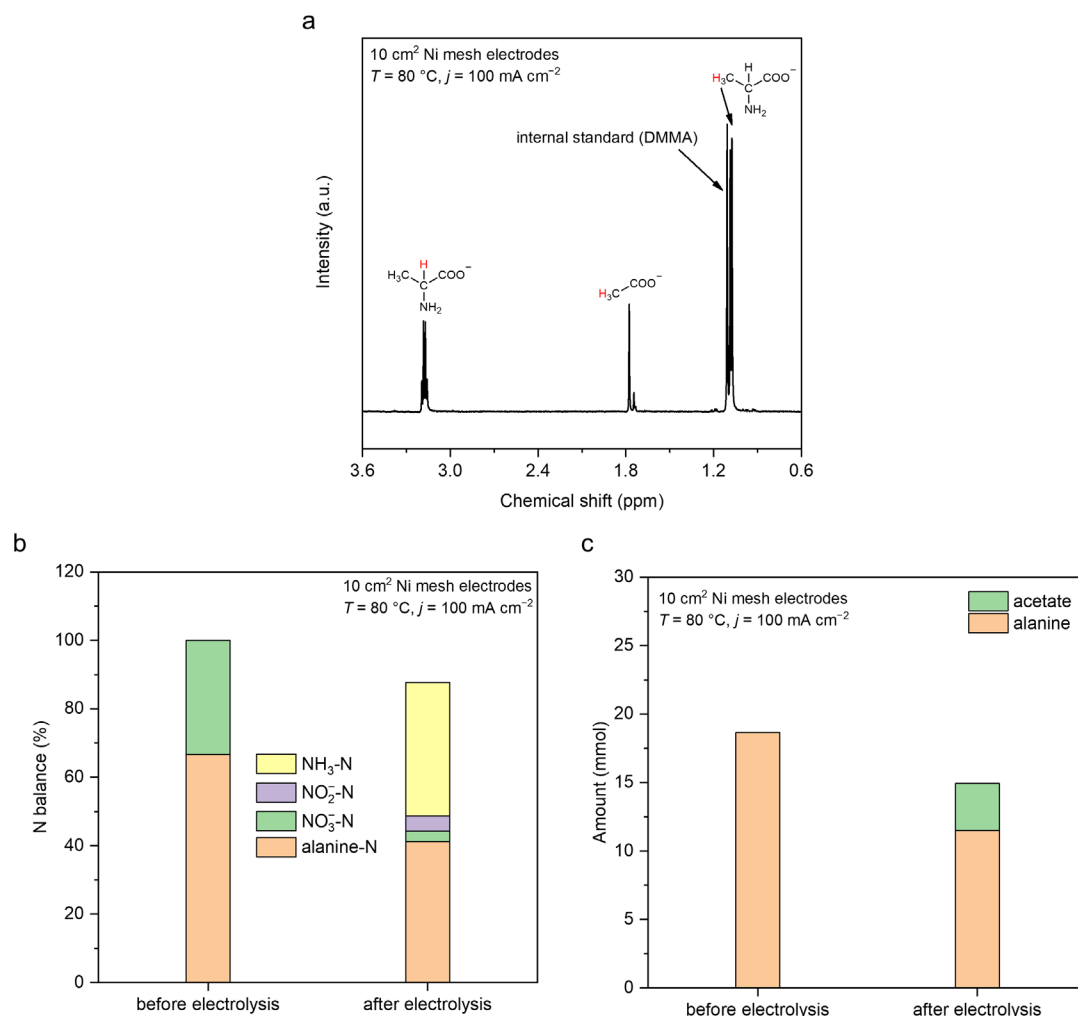
Fig. S40. Quantification of carbon and nitrogen-containing products for the paired electrolysis with KNO_3 and alanine in the $NaOH/KOH/H_2O$ electrolyte. (a) ^1H NMR spectrum of the electrolyte after reaction, showing the protons in the reactant alanine and product acetate. (b) Balance of the nitrogen element. (c) Comparison of the total amount of alanine and acetate before and after electrolysis. Note: before electrolysis, 18.66 mmol of alanine ($C_3H_7NO_2$) and 9.33 mmol of NO_3^- were added into the system; after electrolysis, 11.52 mmol of alanine ($C_3H_7NO_2$), 3.41 mmol of acetate (CH_3COO^-), 0.87 mmol of NO_3^-, and 1.23 mmol of NO_2^- were detected in electrolyte; and 10.94 mmol of NH_4^+ was detected in the absorbing solution. Note that we are unable to quantify CO_3^{2-} in the electrolyte, and we assume its production follows the chemical equation in Fig. S34 (1:1 molar acetate and CO_3^{2-}), which is supported by our qualitative ^{13}C NMR measurement. These results suggest that our system has the carbon and nitrogen elemental balance of ≥80%. None of the volatile carbon-containing products (CO, CH_4, CO_2, C_2H_4, C_2H_2, and C_2H_6) was detected by gas chromatography throughout the electrolysis (Fig. S38). Therefore, the unbalanced portion of carbon and nitrogen could be due to the possible intermediate species unidentified by ^1H NMR, apart from the cumulative measurement errors. Also, further oxidation of acetate to CO_3^{2-} could occur, resulting in the lower apparent carbon balance value. Below are the balances for nitrogen and carbon elements:

The balance of nitrogen element is: $(11.52 + 0.87 + 1.23 + 10.94) \div (18.66 + 9.33) = 87.8\%$

The balance of carbon element is: $(11.52 \times 3 + 3.41 \times 2 + 3.41 \times 1) \div (18.66 \times 3) = 80.0\%$
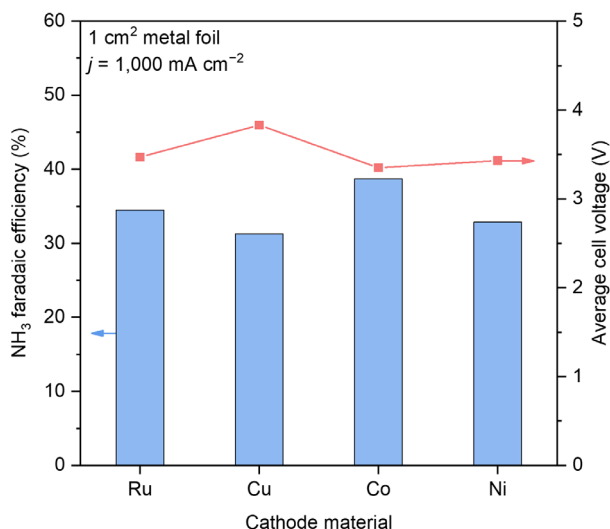
Fig. S41. Comparison of NO3RR performance on different metal foil cathodes in the NaOH/KOH/H$_2$O electrolyte. For a fair comparison, the dimensions of the metal foils were kept identical exactly as 1 × 1 cm^2 and 1 mm thickness. A graphite rod (~8.9 cm^2) was used as the anode to avoid the impact of re-deposited metal species dissolved from the anode. The applied current was 1,000 mA. Note: the FE towards NH$_3$ on four metal foils shows the following trend: Co > Ru > Ni > Cu; and for the average cell voltage: Co < Ni < Ru < Cu. Note that the performance was lower on these metal foils than mesh and foam electrodes, because of the significantly limited surface area available for electrochemical reaction. These results suggest that future development of cathode materials could further improve the cell performance.

4. Supplementary Tables (S1–S3)

Table S1. Summary of state-of-the-art reported performances of NO3RR for electrochemical NH_3 production (sorted by the geometric area-normalized NH_3 production rate).

Ref.	Catalyst	Electrolyte	NH_3 production rate (mol cm^{-2} s^{-1})	$j(NH_3)$ (mA cm^{-2})	FE to NH_3 (%)	Potential/Voltage (V_{RHE})	Cell configuration
this work	commercial Ni foam	NaOH/KOH/H_2O (40 wt.% H_2O)	5.47×10^{-6}	4,220	84.5	4.48 (full cell)	undivided cell
	commercial Ni foam	NaOH/KOH/H_2O (40 wt.% H_2O)	5.87×10^{-7}	453	90.6	3.43 (full cell)	
	commercial Ni mesh	NaOH/KOH/H_2O (40 wt.% H_2O)	1.09×10^{-7}	84.0	84.0	2.56 (full cell)	
[16]	Co-NAs	1 M KOH	2.89×10^{-6}	2,230	98	−0.24	H-cell
[17]	Ru-CuNW	1 M KOH	1.25×10^{-6}	965	93	−0.135	H-cell
[18]	CoO$_x$ nanosheets	0.1 M KOH	5.98×10^{-7}	462	93.4	−0.3	H-cell
[19]	Bi	1 M KOH	3.88×10^{-7}	299	75	−0.8	H-cell
[20]	Cu-N-C	1 M KOH	3.83×10^{-7}	296	95.5	−1	H-cell
[21]	Cu-NBs-100	1 M KOH	3.61×10^{-7}	279	95.8	−0.15	H-cell
[22]	Rh@Cu	0.1 M Na_2SO_4 (pH 11.5)	3.53×10^{-7}	272	69	−0.4	H-cell
[23]	CuPd	1 M KOH	3.47×10^{-7}	268	86.6	−0.6	H-cell
[24]	Fe-cyano NSs	1 M KOH	3.44×10^{-7}	265	90.2	−0.5	H-cell
[25]	Ru-ST-12	1 M KOH	3.25×10^{-7}	251	42	−0.8	H-cell
[26]	CuCoSP	0.1 M KOH	3.25×10^{-7}	251	90.6	−0.175	H-cell
[27]	OD-Cu	1 M KOH	3.06×10^{-7}	236	92	−0.15	H-cell
[28]	CoP NAs	1 M NaOH	2.76×10^{-7}	213	86.2	−0.3	undivided cell
[29]	Cu$_{10}$Ce$_{10}$	1 M KOH	2.75×10^{-7}	212	98.43	−0.23	H-cell
[30]	NiCo$_2$O$_4$/CC	0.1 M NaOH	2.70×10^{-7}	209	95	−0.6	H-cell
[31]	CoFe LDH	1 M KOH	2.58×10^{-7}	199	97.68	−0.45	H-cell
[32]	island-like Cu	0.5 M Na_2SO_4	1.94×10^{-7}	150	98.28	−0.8	H-cell
[33]	ZnCo$_2$O$_4$	0.1 M NaOH	1.76×10^{-7}	136	91.4	−0.8	H-cell
[34]	TiO$_2$	1 M PBS	1.74×10^{-7}	134	80.4	−1.25	H-cell
[35]	Fe$_3$O$_4$/SS	0.1 M NaOH	1.66×10^{-7}	128	91.5	−0.5	H-cell
[36]	Pd(111)	0.1 M Na_2SO_4	1.52×10^{-7}	118	79.91	−0.7	H-cell
[37]	CoO@NCNT/GP	0.1 M NaOH	1.48×10^{-7}	114	93.8	−0.6	H-cell
[38]	pCuO-5	0.05 M H_2SO_4	1.44×10^{-7}	111	68.6	2.2 (full cell)	flow cell
[39]	Fe$_3$C/NC	1 M KOH	1.32×10^{-7}	102	79	−0.5	H-cell
[40]	BCN@Cu	0.1 M KOH	1.28×10^{-7}	98.8	88.9	−0.6	H-cell
[41]	Fe SAC	0.1 M K_2SO_4	1.28×10^{-7}	98.6	66.2	−0.85	H-cell
[42]	Cu$_{50}$Ni$_{50}$/Cu foam	1 M KOH	1.11×10^{-7}	85.5	95	−0.1	flow cell

Table S2. Summary of the results of constant-current NO3RR tests in the NaOH/KOH/H$_2$O electrolyte in this work.

Entry	Added NO$_3^-$ (mmol)	Water content (%)	T (°C)	Cathode	Anode	Electrode area (cm²)	j (mA cm⁻²)	Electrolysis time (h)	Average V_{cell} (V)	NH$_3$ production (mmol)	NO$_3^-$ after rxn (mmol)	FE to NO$_2^-$ (%)	FE to NH$_3$ (%)	X (NO$_3^-$) (%)	N balance (%)
1	9.33	40	80	Ni mesh	Ni mesh	10	100	2	2.56	7.832	0.514	2.33	84.0	94.5	98.7
2	23.32	40	80	Ni mesh	Ni mesh	10	250	2	3.53	21.49	1.052	1.90	92.2	95.5	104.3
3	46.64	40	80	Ni mesh	Ni mesh	10	500	2	3.93	41.08	1.611	2.03	88.1	96.5	99.6
4	139.92	40	80	Ni mesh	Ni mesh	10	500	6	4.01	139.21	1.720	0.35	99.5	95.3	101.0
5	23.32	40	120	Ni mesh	Ni mesh	10	250	2	2.71	17.36	0.483	5.18	74.4	97.9	97.2
6	23.32	40	160	Ni mesh	Ni mesh	10	250	2	2.65	22.45	0.014	1.05	96.3	99.9	100.5
7	9.33	40	200	Ni mesh	Ni mesh	10	100	2	2.08	7.927	0.090	1.09	85.0	99.0	90.3
8	23.32	40	200	Ni mesh	Ni mesh	10	250	2	2.44	21.13	0.205	0.79	90.6	99.1	94.7
9	46.64	40	200	Ni mesh	Ni mesh	10	500	2	3.49	40.13	0.060	0.49	86.0	99.9	88.1
10	9.33	91	80	Ni mesh	Ni mesh	10	100	2	2.87	4.705	3.619	1.67	50.4	61.2	95.9
11	9.33	99	80	Ni mesh	Ni mesh	10	100	2	4.13	3.775	4.476	1.55	40.5	52.0	94.6
12	46.64	40	80	Ni mesh	Ni mesh	4	1,250	2	4.28	44.07	4.302	1.79	94.5	90.8	110.9
13	46.64	40	80	Ni mesh	Ni mesh	1	5,000	2	4.64	32.91	11.74	1.39	70.6	74.8	101.3
14	46.64	40	80	Ni mesh	Ni foam	10	500	2	3.47	40.82	2.578	2.75	87.5	94.5	104.0
15	46.64	40	80	Ni foam	Ni foam	10	500	2	3.43	42.26	1.175	2.76	90.6	97.5	104.2
16	46.64	40	80	Ni foam	Ni mesh	1	5,000	2	4.42	35.41	8.520	1.78	75.9	81.7	101.3
17	46.64	40	80	Ni foam	Ni foam	1	5,000	2	4.48	40.63	8.301	1.61	87.1	82.2	111.3
18	46.64	40	80	Ni foam	Ni foam	1	5,000	2	4.63	40.85	8.485	2.17	87.6	81.8	114.4
19	46.64	40	80	Ni foam	Ni foam	1	5,000	2	4.73	36.75	8.463	2.23	78.8	81.9	105.6
20	46.64	40	80	Ni foam	graphite rod	1 (cathode); 8.9 (anode)	5,000	2	5.85	33.31	6.345	2.46	71.4	86.4	94.8
21	46.64	40	80	Cu mesh	Ni mesh	1	5,000	2	4.86	28.58	12.85	1.16	61.3	72.4	93.5
22[a]	46.64	40	80	Ni mesh	Ni mesh	10	500	2	4.05	40.47	1.741	2.22	86.8	91.1	99.4
23[a]	46.64	40	80	Ni mesh	Ni mesh	10	500	2	3.63	40.85	1.151	1.74	87.6	97.5	97.0
24	9.33	40	80	Ru foil	graphite rod	1 (cathode); 8.9 (anode)	1,000	2	3.47	3.218	5.700	0.19	34.5	38.9	99.4
25	9.33	40	80	Cu foil	graphite rod	1 (cathode); 8.9 (anode)	1,000	2	3.83	2.920	5.939	0.12	31.3	36.3	97.4
26	9.33	40	80	Co foil	graphite rod	1 (cathode); 8.9 (anode)	1,000	2	3.35	3.610	5.613	0.13	38.7	39.8	101.4
27	9.33	40	80	Ni foil	graphite rod	1 (cathode); 8.9 (anode)	1,000	2	3.43	3.066	5.968	0.12	32.9	36.0	99.2

[a] For Entry 22 and 23, air and O$_2$ were used as the carrier gas, respectively. Air was pre-scrubbed in 0.1 M KOH before entering the MFAEL.

Table S3. Summary of the screening test results in the NaOH/KOH/H$_2$O electrolyte in this work. All tests were conducted at 25 mA cm^{-2} at 200 °C, and NH$_3$ was collected every 30 min until no significant increase in its production was detected.

Entry	Added sample	Abbreviation	Structure	N content (wt.%)	Added N (mmol)	NH$_3$ production (mmol)	NH$_3$-N recovery (%)	Electrolysis time (h)
1	(NH$_4$)$_2$SO$_4$	–		21.2	0.207	0.230	111.3	1
2	KNO$_3$	–		13.8	0.201	0.200	99.3	2
3	KNO$_2$	–		16.5	0.222	0.227	102.1	2.5
4	Urea	–		46.6	0.204	0.207	101.3	5
5	Glycine	Gly		18.6	0.205	0.193	94.2	3.5
6	Lysine	Lys		19.2	0.204	0.203	99.4	8.5
7	Arginine	Arg		32.1	0.201	0.190	94.3	8
8	Proline	Pro		12.2	0.216	0.236	109.1	3
9	Ethylenediaminetetraacetic acid	EDTA		9.58	0.201	0.0100	4.99	2[a]
10	Trimethylglycine	TMG		12.0	0.198	0.00436	2.20	2[a]
11	Histidine	His		27.1	0.207	0.224	108.1	4
12	Tryptophan	Trp		13.7	0.188	0.180	95.7	7
13	Adenine	Ade		51.8	0.203	0.190	93.6	6.5
14	Algae powder	–	–	11.5	0.202	0.218	108.0	6.5
15	Protein powder	–		8.90	0.197	0.193	98.0	7

[a] For Entries 9 (EDTA) and 10 (TMG), the electrolysis was terminated at 2 h, because of the very low NH$_3$ production rate.

5. Supplementary References

1. Y. Chen, H. Liu, N. Ha, S. Licht, S. Gu and W. Li, *Nat. Catal.*, 2020, **3**, 1055–1061.
2. D. M. Morales and M. Risch, *J. Phys. Energy*, 2021, **3**, 034013.
3. A. G. Hyder, B. A. Morales, M. A. Cappelle, S. J. Percival, L. J. Small, E. D. Spoerke, S. B. Rempe and W. S. Walker, *Membranes*, 2021, **11**, 217.
4. S.-S. Chou, J.-C. Chung and D.-F. Hwang, *J. Food Drug Anal.*, 2003, **11**, 233–238.
5. J. M. Baker and T. J. Griffis, *J. Environ. Qual.*, 2017, **46**, 1528–1534.
6. A. Rushing, J. Kneifel and B. Lippiatt, *Energy Price Indices and Discount Factors for Life-Cycle Cost Analysis - 2013*, NIST Interagency/Internal Report (NISTIR), National Institute of Standards and Technology, Gaithersburg, MD, 2013.
7. N. W. Rosenberg and C. E. Tirrell, *Industrial & Engineering Chemistry*, 1957, **49**, 780–784.
8. D. A. Vermaas, E. Guler, M. Saakes and K. Nijmeijer, *Energy Procedia*, 2012, **20**, 170–184.
9. S. Pawlowski, J. G. Crespo and S. Velizarov, *J. Membr. Sci.*, 2014, **462**, 96–111.
10. K. M. Chehayeb and J. H. Lienhard, *Environ. Sci. Water Res. Technol.*, 2019, **5**, 1172–1182.
11. Z. Berk, in *Food Process Engineering and Technology (Third Edition)*, ed. Z. Berk, Academic Press, 2018, pp. 193–217.
12. F. Cotana, F. Asdrubali and L. Santarpia, in *International Conference "CFC - The Day After"*, Padova, 1994.
13. B. D. James and D. A. DeSantis, *Manufacturing Cost and Installed Price Analysis of Stationary Fuel Cell Systems*, 2015.
14. W. M. Haynes, *CRC Handbook of Chemistry and Physics*, CRC Press, 2016.
15. D. S. Hall, D. J. Lockwood, C. Bock and B. R. MacDougall, *Proc. Math. Phys. Eng. Sci.*, 2015, **471**, 20140792.
16. X. Deng, Y. Yang, L. Wang, X.-Z. Fu, J.-L. Luo, X. Deng, L. Wang, -Z X Fu, J.-L. Luo and Y. Yang, *Adv. Sci.*, 2021, **8**, 2004523.
17. F.-Y. Chen, Z.-Y. Wu, S. Gupta, D. J. Rivera, S. v. Lambeets, S. Pecaut, J. Y. T. Kim, P. Zhu, Y. Z. Finfrock, D. M. Meira, G. King, G. Gao, W. Xu, D. A. Cullen, H. Zhou, Y. Han, D. E. Perea, C. L. Muhich and H. Wang, *Nat. Nanotechnol.*, 2022, **17**, 759–767.
18. J. Wang, C. Cai, Y. Wang, X. Yang, D. Wu, Y. Zhu, M. Li, M. Gu and M. Shao, *ACS Catal.*, 2021, **11**, 15135–15140.
19. N. Zhang, J. Shang, X. Deng, L. Cai, R. Long, Y. Xiong and Y. Chai, *ACS Nano*, 2022, **16**, 4795–4804.
20. M. Xu, Q. Xie, D. Duan, Y. Zhang, Y. Zhou, H. Zhou, X. Li, Y. Wang, P. Gao and W. Ye, *ChemSusChem*, 2022, **15**, e202200231.
21. Q. Hu, Y. Qin, X. Wang, Z. Wang, X. Huang, H. Zheng, K. Gao, H. Yang, P. Zhang, M. Shao and C. He, *Energy Environ. Sci.*, 2021, **14**, 4989–4997.
22. H. Liu, X. Lang, C. Zhu, J. Timoshenko, M. Rüscher, L. Bai, N. Guijarro, H. Yin, Y. Peng, J. Li, Z. Liu, W. Wang, B. R. Cuenya and J. Luo, *Angew. Chem. Int. Ed.*, 2022, **61**, e202202556.
23. Q. Gao, H. S. Pillai, Y. Huang, S. Liu, Q. Mu, X. Han, Z. Yan, H. Zhou, Q. He, H. Xin and H. Zhu, *Nat. Commun.*, 2022, **13**, 2338.

24. Z. Fang, Z. Jin, S. Tang, P. Li, P. Wu and G. Yu, *ACS Nano*, 2022, **16**, 1072–1081.
25. J. Li, G. Zhan, J. Yang, F. Quan, C. Mao, Y. Liu, B. Wang, F. Lei, L. Li, A. W. M. Chan, L. Xu, Y. Shi, Y. Du, W. Hao, P. K. Wong, J. Wang, S. X. Dou, L. Zhang and J. C. Yu, *J. Am. Chem. Soc.*, 2020, **142**, 7036–7046.
26. W. He, J. Zhang, S. Dieckhöfer, S. Varhade, A. C. Brix, A. Lielpetere, S. Seisel, J. R. C. Junqueira and W. Schuhmann, *Nat. Commun.*, 2022, **13**, 1129.
27. J. Yuan, Z. Xing, Y. Tang and C. Liu, *ACS Appl. Mater. Interfaces*, 2021, **13**, 52469–52478.
28. S. Ye, Z. Chen, G. Zhang, W. Chen, C. Peng, X. Yang, L. Zheng, Y. Li, X. Ren, H. Cao, D. Xue, J. Qiu, Q. Zhang and J. Liu, *Energy Environ. Sci.*, 2022, **15**, 760–770.
29. L. Yang, J. Li, F. Du, J. Gao, H. Liu, S. Huang, H. Zhang, C. Li and C. Guo, *Electrochim. Acta*, 2022, **411**, 140095.
30. Q. Liu, L. Xie, J. Liang, Y. Ren, Y. Wang, L. Zhang, L. Yue, T. Li, Y. Luo, N. Li, B. Tang, Y. Liu, S. Gao, A. A. Alshehri, I. Shakir, P. O. Agboola, Q. Kong, Q. Wang, D. Ma and X. Sun, *Small*, 2022, **18**, 2106961.
31. F. Du, J. Li, C. Wang, J. Yao, Z. Tan, Z. Yao, C. Li and C. Guo, *Chem. Eng. J.*, 2022, **434**, 134641.
32. C. Wang, F. Ye, J. Shen, K.-H. Xue, Y. Zhu and C. Li, *ACS Appl. Mater. Interfaces*, 2022, **14**, 6680–6688.
33. Z. Li, J. Liang, Q. Liu, L. Xie, L. Zhang, Y. Ren, L. Yue, N. Li, B. Tang, A. A. Alshehri, M. S. Hamdy, Y. Luo, Q. Kong and X. Sun, *Mater. Today Phys.*, 2022, **23**, 100619.
34. Y.-T. Xu, Z. Peng, Y. Han, H. Zhong, J. Yang and Y. Cao, *ChemSusChem*, 2022, **15**, e202102450.
35. X. Fan, L. Xie, J. Liang, Y. Ren, L. Zhang, L. Yue, T. Li, Y. Luo, N. Li, B. Tang, Y. Liu, S. Gao, A. A. Alshehri, Q. Liu, Q. Kong and X. Sun, *Nano Res.*, 2022, **15**, 3050–3055.
36. Y. Han, X. Zhang, W. Cai, H. Zhao, Y. Zhang, Y. Sun, Z. Hu, S. Li, J. Lai and L. Wang, *J. Colloid Interface Sci.*, 2021, **600**, 620–628.
37. Q. Chen, J. Liang, L. Yue, Y. Luo, Q. Liu, N. Li, A. A. Alshehri, T. Li, H. Guo and X. Sun, *Chem. Commun.*, 2022, **58**, 5901–5904.
38. R. Daiyan, T. Tran-Phu, P. Kumar, K. Iputera, Z. Tong, J. Leverett, M. H. A. Khan, A. Asghar Esmailpour, A. Jalili, M. Lim, A. Tricoli, R. S. Liu, X. Lu, E. Lovell and R. Amal, *Energy Environ. Sci.*, 2021, **14**, 3588–3598.
39. Y. Wang, L. Zhang, Y. Niu, D. Fang, J. Wang, Q. Su and C. Wang, *Green Chem.*, 2021, **23**, 7594–7608.
40. X. Zhao, G. Hu, F. Tan, S. Zhang, X. Wang, X. Hu, A. v Kuklin, G. v Baryshnikov, H. Ågren, X. Zhou and H. Zhang, *J. Mater. Chem. A*, 2021, **9**, 23675–23686.
41. Z.-Y. Wu, M. Karamad, X. Yong, Q. Huang, D. A. Cullen, P. Zhu, C. Xia, Q. Xiao, M. Shakouri, F.-Y. Chen, J. Y. (Timothy) Kim, Y. Xia, K. Heck, Y. Hu, M. S. Wong, Q. Li, I. Gates, S. Siahrostami and H. Wang, *Nat. Commun.*, 2021, **12**, 2870.
42. Y. Wang, A. Xu, Z. Wang, L. Huang, J. Li, F. Li, J. Wicks, M. Luo, D.-H. Nam, C.-S. Tan, Y. Ding, J. Wu, Y. Lum, C.-T. Dinh, D. Sinton, G. Zheng and E. H. Sargent, *J. Am. Chem. Soc.*, 2020, **142**, 5702–5708.